



Original Paper

Estimation of Petrophysical Parameters from Seismic Inversion by Combining Particle Swarm Optimization and Multilayer Linear Calculator

Qamar Yasin,^{1,2} Ghulam M. Sohail,³ Yan Ding,^{1,2,4} Atif Ismail,⁵ and Qizhen Du^{1,2,6}

Received 23 July 2019; accepted 15 February 2020
Published online: 2 March 2020

In heterogeneous reservoir rocks, the accurate characterization of lithology and reservoir parameters is significant to minimize drilling risks and to improve oil and gas recoveries. In this work, a joint inversion strategy based on multilayer linear calculator (MLC) and particle swarm optimization (PSO) algorithm was applied to predict the spatial variations of key petrophysical (porosity, permeability, and saturation) and geomechanical parameters (Young's modulus, Poisson's ratio, and brittleness) for inter-well regions. In this method, acoustic impedance (AI) models are computed from post-stack seismic amplitude data by applying the proposed strategy (MLC + PSO) and back propagation neural network-based seismic inversion in the time domain with measured log density and velocity as constraints. The obtained results reveal that the proposed strategy, which combines MLC and PSO, leads to the optimization of lateral and vertical facies heterogeneities and accurate prediction of reservoir parameter distribution, i.e., the low AI is related to sand facies and corresponds to high porosity, permeability, saturation, and mid-range of Young's modulus. The time slice maps of inverted porosity and permeability at various time intervals indicate a reasonable calibration with the measured core and well log data. The methodology proposed in this study may be considered useful for other basins in Pakistan with similar geological settings and anywhere in the world for reservoir characterization, particularly for intercalated shale and variable depositional environments.

KEY WORDS: Reservoir characterization, Particle swarm optimization, Multilayer linear calculator, Petrophysical modeling.

INTRODUCTION

In the past few decades, acoustic impedance (AI) mapping obtained from the inversion of post-stack seismic amplitude data has become a common approach to predict spatial reservoir properties. The inverted models of AI, i.e., P-impedance, S-impedance, and density, can be further used for the estimation of lithofacies, petrophysical, and elastic parameters (Leiphart and Hart 2001; Walls et al. 2002; Pramanik et al. 2004; Calderon 2007; Singha and Chatterjee 2014; Kumar et al. 2016). In the lit-

¹The Key Laboratory of Deep Oil and Gas, China University of Petroleum (East China), Changjiang West Road 66th, Qingdao 266580, China.

²The Laboratory for Marine Mineral Resources, Qingdao National Laboratory for Marine Science and Technology, Qingdao 266071, China.

³Department of Civil, Geological and Environmental Engineering, University of Saskatchewan, Saskatoon, Canada.

⁴Beijing Rock Star Petroleum Technology Co., LTD, Beijing 102200, China.

⁵Department of Geological Engineering, University of Engineering and Technology, Lahore, Pakistan.

⁶To whom correspondence should be addressed; e-mail: multicomponent@163.com

erature, two broad seismic inversion categories have been discussed: a) pre-stack seismic inversion (fluid indicator) and b) post-stack seismic inversion (rock indicator) (Ali et al. 2018). For a seismic inversion specialist, the most important task includes pre-stack seismic inversion and interpretation of AVO analysis (i.e., seismic amplitude variations with offset). From pre-stack data, the preserved angular information is employed to predict lithological and fluid properties with more reliability. The pre-stack data can be instantly available because of easy access and low time-consuming processing but difficult to obtain in all fields. In recent years, a wide variety of applications of post-stack seismic inversion algorithms for conventional and unconventional reservoir parameter estimations has been reported in the literature (Kumar et al. 2016; Chatterjee et al. 2016; Golsanami et al. 2019). Seismic inversion is therefore used as one of the most predictive tools for reservoir parameters and delineation of facies in oil and gas explorations. Wells drilled in a field are spaced more than hundreds to thousands of meters apart; hence, seismic inversion can aid in predicting important reservoir properties among the wells. The integration of seismic and well data can therefore significantly improve the distribution of reservoir properties for the inter-well region. The ultimate goal of seismic inversion is the transformation of seismic reflection data into AI to aid in providing information related to spatial reservoir properties, such as porosity, permeability, saturation, Young's modulus, Poisson's ratio, and brittleness index (Russell 2004; Sancevero et al. 2005; Soubotcheva 2006; Das and Chatterjee 2018a, b; Gogoi and Chatterjee 2019).

Mechanical factors are evaluated in a region with high Young's modulus, low Poisson's ratio, and abundant natural fractures (Rickman et al. 2008; Aybar et al. 2015; Yasin et al. 2017, 2018; Das and Chatterjee 2018a, b). The seismic-derived dynamic Young's modulus and Poisson's ratio indicate the lateral changes in elastic moduli and brittleness related to the wellbore stability analysis and fractured zones (Charlez 1997; Rickman et al. 2008; Das and Chatterjee 2018a, b).

In the last few decades, several methods and algorithms have been developed for mapping the AI from post-stack seismic amplitude data and further linked to estimate the distribution of reservoir properties in space (Russell 1988, 2004). At present, the increase in computing power and the modern assistance of acquisition, processing, and interpre-

tation of seismic data enable reservoir geophysicists to focus on machine learning, i.e., AI extraction using neural network algorithm (Walls et al. 2002; Pramanik et al. 2004; Calderon 2007; Demuth et al. 2008). The main advantages of artificial neural networks over traditional statistical inversions are briefly discussed as follows. (1) Artificial neural networks have the ability to derive nonlinear relationships between target values and input data; (2) it is less sensitive to noisy data; (3) there is no apprehension in using the underlying statistical distribution of input data. The neural network algorithms can therefore be successfully applied to extract AI and additional information on detailed reservoir characterization from post-stack seismic inversion (Hampson et al. 2001; Walls et al. 2002; Pramanik et al. 2004; Calderon 2007; Golsanami et al. 2015).

The artificial neural network method, such as the back propagation (BP) neural network, however, has a single network structure, resulting in strong randomness and reduced nonlinear representation ability (over fitting). Moreover, the genetic algorithm does not have real global superiority optimization that leads to the convergence of local minimum and extreme randomness. To resolve the foregoing nonlinear problems, Ding et al. recently developed an improved multilayer linear calculator (MLC) inversion model (unpublished work). In this particular study, to optimize performance, the MLC inversion model was used with the particle swarm optimization (PSO) algorithm. Different from genetic algorithms, the PSO has a more straightforward 'velocity' equation by setting a series of independent particles to search the designed space. It is a new global optimization approach to afford the advantages of strong robustness for local search ability and good scalability, which can be realized easily with fewer parameter adjustments (Singh and Biswas 2016).

In the under-explored middle Indus basin, the remaining potential gas reservoirs were evaluated using current techniques, such as well logs, geological modeling, and seismic data characterization (Droz and Bellaiche 1991; Ali et al. 2018). In recent years, Sheikh and Giao (2017) evaluated the middle Indus basin as a shale gas potential in the deeper Cretaceous sections (Appendix, Fig. 24). The Cretaceous sandstone of the Lower Goru Formation is the main deposited reservoir. It is of heterogeneous shallow marine origin from a proximal delta-front environment and divided into A, B, C, and D sand intervals (Quadri 1986; Ahmad et al. 2004).

In the Lower Goru Formation, the discrimination between lateral and vertical facies heterogeneities and spatial distribution of reservoir parameters is considered problematic. A recent study performed by Ali et al. (2018) indicated that model-based post-stack inversion can provide satisfactory results for the spatial distribution of reservoir properties and demarcation of potential gas-saturated zones in the C-sand interval of the Lower Goru Formation. The model-based inversion algorithm, however, was unable to capture the thin shale layers and channel sandstone from shale in the C-sand interval in the formation. Moreover, the lateral and vertical facies heterogeneities and reservoir parameter distribution were not calibrated with measured data and signature analysis.

To solve the problems of facies heterogeneity, clustering algorithms, such as self-organizing maps (SOM) (Moqbel and Wang 2011; Kiaei et al. 2015), have been employed in the Lower Goru Formation to analyze the facies distribution using combined facies discrimination logs. As demonstrated in the previous work of the authors (Du et al. 2019), the SOM has an effective performance on facies analysis in a heterogeneous reservoir because it does not have any difficulty in dealing with a broad range of facies heterogeneity. The Gaussian-indicating algorithm has been utilized then to perform the lateral and vertical variation of SOM facies analysis.

The framework of this study is organized as follows. (a) A detailed interpretation of three-dimensional (3D) seismic data was conducted to mark the top and bottom horizons of the C-sand interval of the Lower Goru Formation. Figure 1 shows a 3D seismic cube covering the top and bottom horizons

of the target interval within a specified time window (2100–2400 ms). (b) The synthetic seismogram was calibrated with seismic data to locate and trace the target reservoir interval. (c) Finally, the proposed strategy (MLC + PSO) was applied to predict the spatial distribution of AI and important reservoir parameters for the inter-well regions.

The focus of this study was on the C-sand interval of the Lower Goru Formation as the main gas-producing reservoir in the middle Indus basin. The inverted seismic porosity, permeability, saturation, Young's modulus, Poisson's ratio, and BI interpretations are extended, however, deeper into the late Cretaceous Sembar Formation to evaluate the shale gas potential (Appendix, Fig. 24). The main objective, nevertheless, was to compare and contrast the proposed strategy (MLC + PSO) with BP neural network inversion algorithms and evaluate the remaining potential of C-sand interval. Furthermore, new information on the deeper horizon of the Cretaceous Sembar shale was provided for the unconventional play in the study area.

GEOLOGICAL MODELING OF THE STUDY AREA

The Sawan gas field is one of the largest located in the middle Indus basin, Pakistan (Appendix, Fig. 24). The highest expected recovery of 1 tcf (374.75 m³) from Sawan gas field ranks the middle Indus basin among the main hydrocarbon-producing basins in Pakistan (Berger et al. 2009; Ahmed et al. 2013). The minimal reservoir quality and dipping structure are the leading causes of hydrocarbon

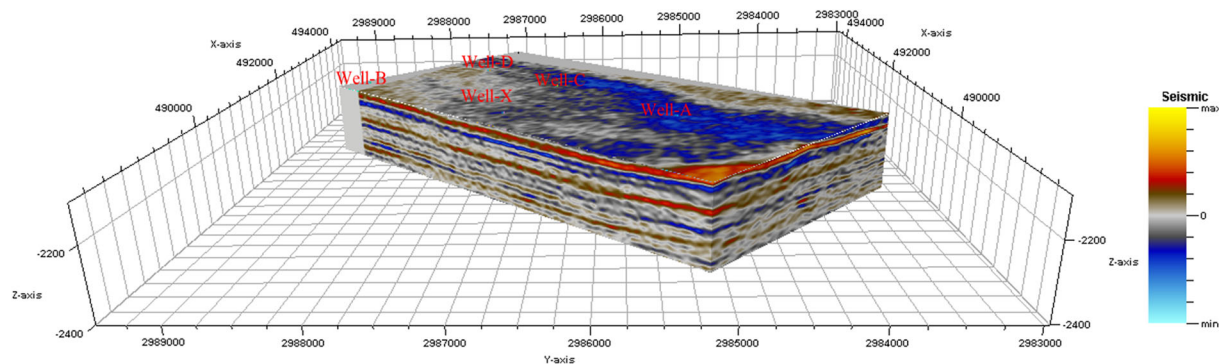


Figure 1. 3D seismic cube covering target horizons, including the inline and cross-line traces, within a specified time window (2100–2400 ms).

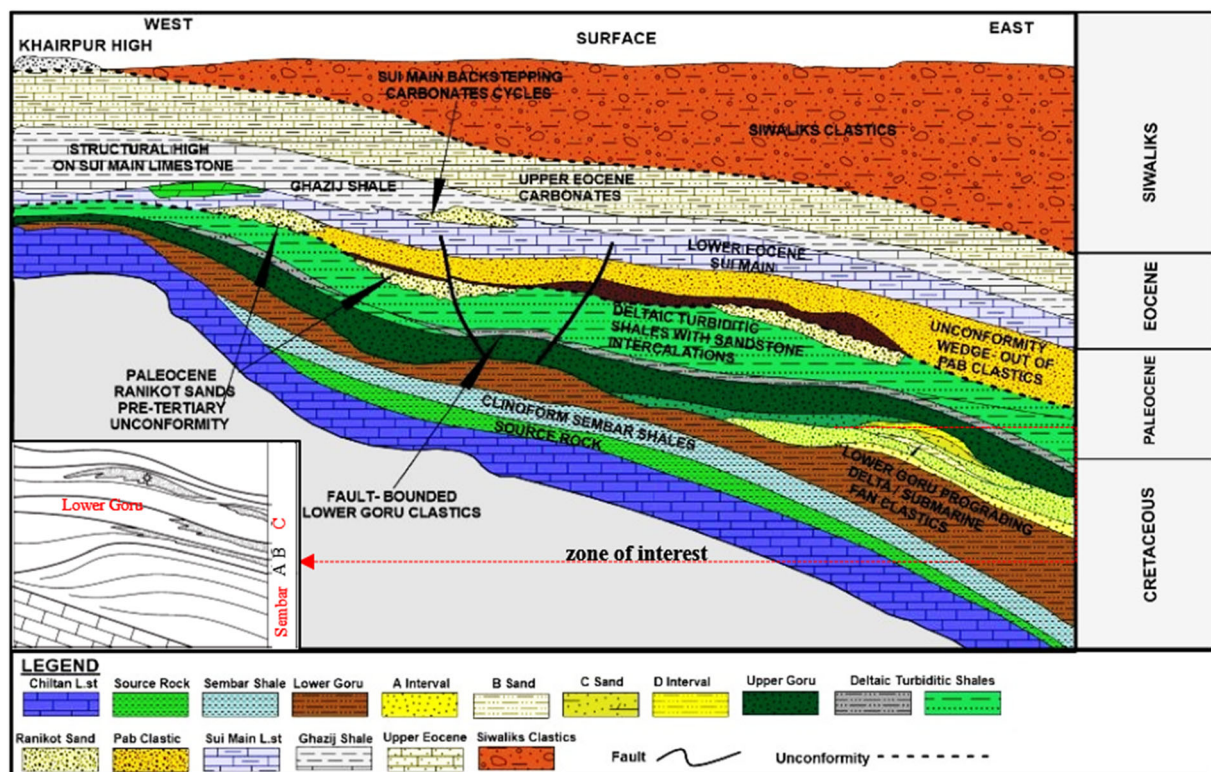


Figure 2. Regional geological model indicating stratigraphic sequences and facies architecture in study area (Milan and Rodgers 1993; Khan et al. 1999).

trapping mechanisms in this gas field (Quadri 1986). Based on petrographical studies and well log evaluation, the regional geological model was prepared to understand the sedimentary environment, facies architecture, and stratigraphic sequences in the study area (Fig. 2). According to the regional geological model, the stratigraphy sequence was identified from the deeper Chiltan limestones (exposed or drilled) of the Jurassic, overlain by the Sembar and Lower Goru Formations of the Cretaceous, and followed by rocks ranging in age up to the Quaternary. During the variable duration, a stratum erosion was identified between the Chiltan limestones and the lowermost Sembar and Lower Goru Formations. A time gap of approximately 30 million years was present between the Sembar and the Lower Goru Formation (Berger et al. 2009). In the middle Indus basin, the organic-rich shales of Sembar Formation act as a major source rock for sandstones of the Lower Goru Formation. The sandstones of the Lower Goru Formation is divided (from bottom to top) into A, B, and C intervals

(Berger et al. 2009). These reservoir sands are dipping and prograding toward the east (Fig. 2). The intended zone of interest, the C-sand interval, lies at the shallow marine region of the depositional up-dip low-stand wedge. The developed geological model indicates that the heterogeneity in the lateral and vertical facies distributions is significantly affected by the variable depositional environment of the Lower Goru Formation. The depositional environments of the Lower Goru Formations suggest deltaic channels, prograding delta-distributaries, and delta-front settings (Ashraf et al. 2018). In horizons A, B, and C sand intervals are composed of coarsening-upward shoreline packages, and dominant progrades (Ashraf et al. 2018). Quartz is the major mineral constituent present in the reservoir interval with minimal amounts of feldspar grains (orthoclase, microcline, and plagioclase), igneous rock fragments (volcanic glass, accessory mineral, tourmaline, and monazite), chlorites, and micas (Berger et al. 2009; Yasin et al. 2019). Micas, which are also present within the delta sequences, represent the deposition

in the inter-fingering of the prograding distributary channels into the distributary mouth bars. This could be correlated with the depositional setting in the coarsening-upward trend of delta front. The sediments deposited above the 3340-m depth, as defined by the gamma-ray log signature, suggest a possible shallow marine origin of the proximal delta-front setting (Fig. 5).

The stratigraphic analysis performed in previous studies (Yasin et al. 2019) indicates that the C-sand interval thickness varies from 90 to more than 100 m, whereas that of clean sandstone is 67–82.25 m. The high frequency of thick sandstone beds from 3250 to 3330 m in Well-A and from 3270 to 3340 m in Well-C and Well-D represent the prograding delta associated with the fall of sea level. The overall thickness of the sandstone layer decreases from the northeast (NE) toward the southwest (SW). These sandstone layers therefore have a significant gas potential in the reservoir interval. In particular, at the bottom of the reservoir interval, the percentage of marine shale and lime mud siltstone/claystone suggests a lower shoreface compared with the offshore fine sediments along the basin-ward depositional environment. These shale, silts, and tight sands at the bottom of the reservoir interval can act as unconventional play (Ashraf et al. 2018).

WELL LOG AND SEISMIC DATASETS

In this study, log data from five production wells, A, B, C, D, and E were used for the estimation of petrophysical and geomechanical properties in the C-sand interval. Gamma ray (GR), spontaneous potential (SP), calliper, deep resistivity (LLD), P and S wave sonic (DT_P and DT_S), density (RHOB), and neutron porosity (NPHI) logs were analyzed to detect new hydrocarbon-bearing zones and reservoir modeling from the five wells. In the literature, 237 core samples from the C-sand interval of the Lower Goru Formation were available for calibrating the estimation of permeability and porosity (Table 1). 3D seismic data covering approximately 200 km² were also available. The two horizons, top and bottom of the C-sand interval, were interpreted on these seismic data.

Table 1. Routine core analysis data of permeability and porosity in Well-C and Well-B, respectively

Depth (m)	Permeability (mD)	Porosity (%)
3269	1507.53	24.58
3272	1842.84	24.75
3274	5726.47	27.61
3277	3911.47	28.78
3279	2508.36	27.96
3280	681.75	29.44
3282	2389.74	26.62
3284	9894.10	31.43
3285	5132.04	29.32
3287	6574.01	30.99
3288	3860.73	29.72
3290	956.70	29.57
3293	9522.14	30.87
3301	1539.83	22.34
3312	858.14	22.49
3321	140.58	27.44
3325	50.21	22.50
3331	0.02	6.58
3335	0.05	11.90
3338	0.22	14.83
3395	1134.00	25.65
3407	230.45	25.01
3423	649.10	25.14
3447	7.66	14.38

POST-STACK SEISMIC INVERSION: METHODOLOGY

Estimation of Reservoir Parameters

The initial phase in the context of this work involves the estimation of petrophysical and geomechanical parameters to identify the unexplored hydrocarbon-bearing zones in the reservoir interval. The subsequent equations were employed to estimate the effective porosity, permeability, hydrocarbon saturation, Young’s modulus, Poisson’s ratio, and brittleness index (BI). The results are compared with laboratory-measured porosity and permeability data, as summarized in Table 1.

The shale volume (V_{sh}) is estimated from the GR log using Eq. 1:

$$V_{sh} = \frac{GR_{log} - GR_{min}}{GR_{max} - GR_{min}} \tag{1}$$

where GR_{log} , GR_{min} , and GR_{max} are the gamma-ray log reading in the zone of interest, 100% clean sand, and 100% shale, respectively, (API units).

The total porosity is estimated using the density log in Eq. 2:

$$\varphi = \frac{\rho_{ma} - \rho_b}{\rho_{ma} - \rho_f} \quad (2)$$

where ρ_{ma} and ρ_f are the matrix density and fluid density, respectively.

The effective porosity (ϕ_{eff}) was estimated using the shale volume (V_{sh}) and total porosity (ϕ) from Eqs. 1 and 2.

$$\phi_{eff} = \phi_D(1 - V_{sh}) \quad (3)$$

Using Eqs. 1, 2, and 3, the water saturation (S_w) can be calculated using the Poupon-Leveaux Indonesian model:

$$S_w = \left\{ \left[\left(\frac{V_{sh}^2 - V_{sh}}{R_{sh}} \right)^{\frac{1}{2}} + \left(\frac{\varphi_e^2}{R_w} \right)^{\frac{1}{2}} \right]^2 R_t \right\}^{-1/2} \quad (4)$$

$$S_h = 1 - S_w \quad (5)$$

where R_t is the true resistivity of the formation obtained from the LLD log response; R_{sh} is the resistivity of shale (4 Ωm); R_w is the resistivity of water formation (0.5 Ωm).

The permeability of the C-sand interval was estimated based on the previous work of the authors (Yasin et al. 2019) that combines the neural network with multiple regression to predict accurate permeability values. This approach was also applied in this work. The proposed equation is as follows.

$$\text{Estimated Permeability} = 10^{-2.6+0.027 \times GR+4 \times \text{Log(LLD)}-0.38 \times RHOB-11.09 \times NPHI} \quad (6)$$

Young's modulus (E_d), in GPa, and Poisson's ratio (ν_d) are estimated using shear (V_s) and compressional (V_p) wave velocity and bulk density (ρ_b) (Mavko et al. 2009).

$$E_d = \rho_b V_s^2 \left(\frac{3V_p^2 - 4V_s^2}{V_p^2 - V_s^2} \right) \times 10^{-6} \quad (7)$$

$$\nu_d = \frac{1}{2} \left(\frac{V_s^2 - 2V_p^2}{V_s^2 + V_p^2} \right) \quad (8)$$

The bulk modulus (K) can be calculated by an empirical relationship that uses dynamic E_d and ν_d (Archer and Rasouli 2012).

$$K = \frac{E_d}{3(1 - 2\nu_d)} \quad (9)$$

The shear modulus (G) is estimated using ρ_b and V_s (Mavko et al. 2009).

$$G = \rho_b V_s^2 \quad (10)$$

Rickman et al. (2008) derived a formula for estimating BI (*Brittleness Index*):

$$E_{\text{Brittleness}} = \frac{E - E_{\min}}{E_{\max} - E_{\min}} \quad (11)$$

$$\nu_{\text{Brittleness}} = \frac{\nu - \nu_{\min}}{\nu_{\max} - \nu_{\min}} \quad (12)$$

$$\text{Brittleness Index} = \frac{E_{\text{brittleness}} - \nu_{\text{brittleness}}}{2} \quad (13)$$

where $E_{\text{brittleness}}$ = brittleness from E_d , $E_{\max} = E_d$ (maximum), and $E_{\min} = E_d$ (minimum); $\nu_{\text{brittleness}}$ = brittleness from ν_d , $\nu_{\max} = \nu_d$ (maximum), and $\nu_{\min} = \nu_d$ (minimum).

Multilayer Linear Calculator Inversion Model

The MLC inversion model is composed of multiple linear calculators and domain gates that can divide a complex function into simple linear ones

with the domain gate controlling the output weight of each layer. Specifically, a function in one dimension can be divided into several linear segments, whereas a two-dimensional function can be divided into a number of facets with this calculator. Based on the linear segmentation approximation, the nonlinear inversion problem is converted to estimate the weights of several linear calculators.

Suppose that \mathbf{y}^* is a set of reservoir parameters calculated from the numerical models in the reservoir interval obtained by applying Eqs. 2–6 and 12–13, and suppose that \mathbf{x} is the collection of seismic

records. The two parameters are connected by the projection operator, Ω .

$$A^* = (B) \tag{14}$$

The relationship Ω between the two variables (x and y^*) is injective and nonlinear. For the minimum expected risk, an optimum response function could be found

$$\phi(B) = \sum_{i=1}^m (A_i(B) - A_i^*(B))^2 \tag{15}$$

where $\phi(x)$ is the objective function or adaptive value; m is the number of target; $y_i(x)$ is the value of the learning data, x , with MLC; $y_i^*(x)$ is the real corresponding value of the learning data.

The MLC is an operator of a single input-desired output with n corresponding to the length of seismic data. In this inversion model, the input sample (x) is weighted-stacked and added to bias b , as shown in Eq. 16.

$$A = f\left(\sum_{i=0}^n B_i w_i + b\right) \tag{16}$$

where f in the formula is an activation function that represents the designed domain gates and it can be calculated using Eq. 17:

$$f = \frac{1}{1 + \sum_{i=1}^l \exp(-\sum_{i=0}^n B_i w_i + b)} \tag{17}$$

where ‘ l ’ is the number of linear calculators.

The weight of each MLC inversion model, which includes the bias, was determined by the PSO algorithm (Parsopoulos and Vrahatis 2004). The relationship between the MLC and PSO algorithm is presented in Figure 3.

For an input learning value, x (seismic waveform), the MLC inversion model can first be utilized to calculate the output, y . In order to satisfy the nonlinear projection relationship with real y^* (reservoir parameters from well logs), the PSO algorithm was employed to optimize the MLC inversion model and calculate the appropriate weight. Stable prediction results with the appropriate weight can thereafter be obtained.

PSO Algorithm

The PSO is a new global convergence algorithm that is used to provide excellent convergence rates for different optimization problems. In this study, the PSO was combined with the MLC inversion for conjunctive inversion of seismic data. First, model parameterization (i.e., number of arc-tangent nodes and layers, the number of individuals (or particles), search limits for each component, and stopping criteria) was determined.

Suppose that the PSO consists of M particles with D dimension; the parameters for every particle at each moment are denoted as follows.

The particle location is represented by $X_i^t = (X_{i1}^t, X_{i2}^t, \dots, X_{id}^t)^T$, $X_{id}^t \in [L_d, U_d]$, where U_d

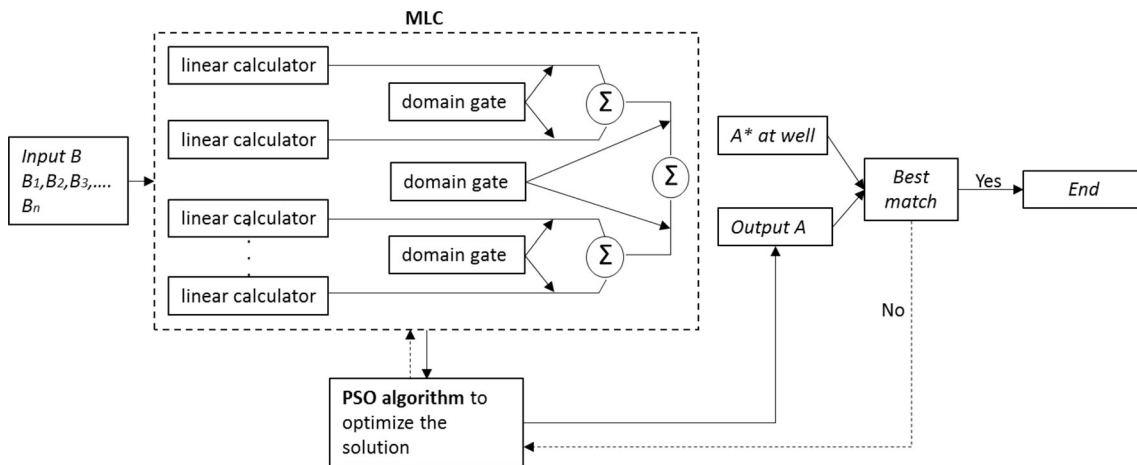


Figure 3. Multilayer linear calculator and particle swarm optimization algorithms inversion scheme.

and L_d are the upper and lower limits of search space, respectively.

The velocity is $V_i^t = (V_{i1}^t, V_{i2}^t, \dots, V_{id}^t)^T$ and $V_{id}^t \in [V_{\min,d}, V_{\max,d}]$, where $V_{\max,d}$ and $V_{\min,d}$ denote the maximum and minimum velocities, respectively. The ranges of parameters i and d are $1 \leq d \leq D, 1 \leq i \leq M$.

The individual optimal position is labeled as $p_i^t = (p_{i1}^t, p_{i2}^t, \dots, p_{iD}^t)^T$, and the global optimal positions, $p_g^t = (p_{g1}^t, p_{g2}^t, \dots, p_{gD}^t)^T$, are the positions of the particle swarm after the update of each iteration. The parameters at time $t + 1$ can be computed by Eqs. 18 and 19:

$$V_{id}^{t+1} = \omega V_{id}^t + c_1 r_1^t (P_{id}^t - X_{id}^t) + c_2 r_2^t (P_{gd}^t - X_{gd}^t) \quad (18)$$

$$X_{id}^{t+1} = X_{id}^t + V_{id}^{t+1} \quad (19)$$

where c_1 and c_2 are the learning factors that control the relative proportion of cognition and social interaction; ω is the inertia weight used as a memory of previous velocities that can balance the effects between global search and local search.

For the implementation, $l = 5$, particle number = 100, learning factors $c_1 = c_2 = 2$, inertia weight $\omega = 1$, lower limit $L_d = -3$, and upper limit $U_d = 3$. The maximum velocity was $V_{\max} = 0.08$, the number of iterations was $T_{\max} = 200$, and precision was $e = 0.1$. With a calculation precision of 89% and computation time of 5 min, these parameters are proved efficient for convergence.

The workflow for predicting reservoir parameters using MLC and PSO inversion algorithms is described as follows.

1. The learning seismic data that contain well information are arranged and labeled as $\mathbf{x} = (\mathbf{x}_1, \mathbf{x}_2, \mathbf{x}_3, \dots, \mathbf{x}_n)$; the PSO was composed of all samples of the seismic data. The corresponding reservoir parameters from well logs calculated according to the Eqs. 2–6, and 12–13 are labeled as \mathbf{y}^* .
2. The search space parameters, including the minimum velocity (V_{\min}) and maximum velocity (V_{\max}), learning factors c_1 and c_2 , maximum iteration number (T_{\max}), highest convergence precision (e), weight (ω), and individual and global optimal positions are artificially set. The location parameters (x_i)

and velocity (V_i) are randomly initialized through the seismic data of nearby wells according to Eqs. 18 and 19.

3. The MLC was employed to match the target reservoir parameters. In particular, the location parameters (all samples of seismic data) were estimated by Eq. 16, and the output was labeled as \mathbf{y} .
4. The parameters (output \mathbf{y} calculated in step 3 and measured data, \mathbf{y}^*) are substituted into the optimum response function, Eq. 5.
5. According to the minimum principle of the objective function, the location and individual optimum parameters (X_i and p_i , respectively) are first updated, followed by the global optimum, p_g . If the global optimal value (\mathbf{g}_{best}) matches the highest precision, e , then the iteration will be terminated; otherwise, iteration continues.
6. The conditions of iteration are examined. The calculation will be terminated if T_{\max} is smaller than the current iteration number; the result is the current global optimum. Otherwise, revert to step 3.

RESULTS AND DISCUSSION

Petrophysics

As previously discussed, the first stage of reservoir characterization is the transfer of the raw data, which include wellbore information and reliable petrophysical properties to identify the hydrocarbon-bearing zones in the reservoir interval. Figure 4 shows the well correlation, indicating the facies distribution within the C-sand interval using the GR log from the wells under study. In the upper part of the reservoir, the GR values were in the range 45–80 API with sandstone as the dominant lithology. In contrast, the high GR values in the lower part indicate that shale is the dominant lithology. Several thin sand–shale layers can also be observed in the whole reservoir interval. The discontinuity in the reservoir lithofacies toward Well-E is caused by the anticipated heterogeneities and complexities in the region (Ashraf et al. 2018). The moderate-to-high GR values in Well-B indicate shaley sandstone to shale lithofacies.

Figure 5 shows the interpreted profiles of the reservoir interval, including porosity, permeability,

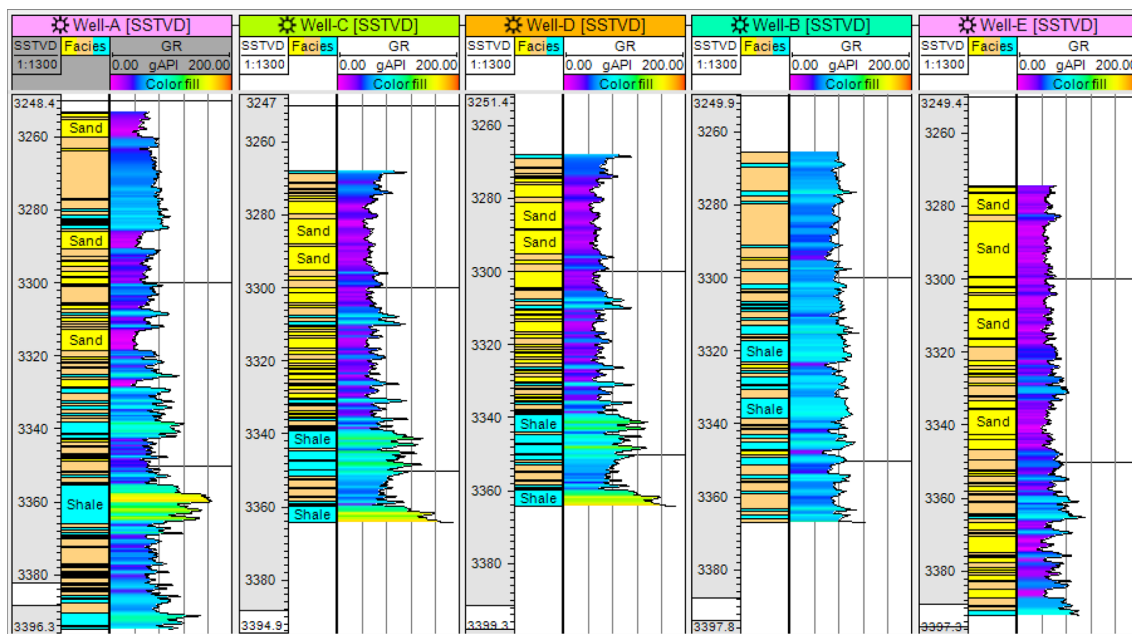


Figure 4. Cross section of well correlation indicating vertical variation in lithofacies and generalized lithology of studied formation.

gas content, Young’s modulus, Poisson’s ratio, and brittleness index (BI) for the five wells in the Sawan area.

In Well-C (Fig. 5), the routine core analysis data of 237 samples were used to assess the level of correlation between estimated and measured petrophysical properties. The correlation coefficient between measured and estimated permeabilities (Eq. 6) is high, i.e., $R^2 = 0.97$ (Appendix, Fig. 25). As shown in track-2 of Well-C, a good agreement between measured and estimated permeabilities was observed from the top to the 3280-m interval; however, the permeability significantly varies at the bottom because of the extreme heterogeneity in the facies. The estimated porosity in Well-C (track 3) agreed well with measured porosity data throughout the interval, implying that compared with permeability, the porosity was less sensitive to heterogeneity.

In Well-B, the hydrocarbon saturation was high (up to 60%) from the top to the 3304-m deep interval. Along the reservoir sections at depths in the range 3304–3355 m, the values of hydrocarbon saturation, porosity, and permeability zones were low. It should be noted that there was an abrupt change in the hydrocarbon saturation below the 3355-m depth. The low value of hydrocarbon satu-

ration in the depth range 3304–3355 m is caused by several sandy shale and shale layers present in this interval (Fig. 4). It is important to note that a good correlation exists between the estimated and measured petrophysical properties (tracks 2 and 3). The elastic moduli, Young’s modulus, shear modulus, and bulk modulus were consistent: They decrease with the increase in porosity and permeability (track 4).

In Well-A, the average value of hydrocarbon saturation was 30% from the top to the bottom of the reservoir interval. The dominant lithologies in Well-A are shaley sandstone and sandstone facies, which are more related to the moderate-to-high permeability and porosity. Note that the porosity and permeability trends were inconsistent throughout the reservoir interval, indicating significant heterogeneities in Well-A. The elastic moduli in the upper part of the reservoir interval were relatively low but gradually increased with depth. The low values of Young’s, shear, and bulk moduli are caused by the high shaley content. The elastic moduli and saturation has a reverse correlation, i.e., the increase in saturation causes the decrease in elastic moduli.

In Well-D, permeability and porosity followed the same trends but gradually decreased with decrease in sandy layers and increased in shale litho-

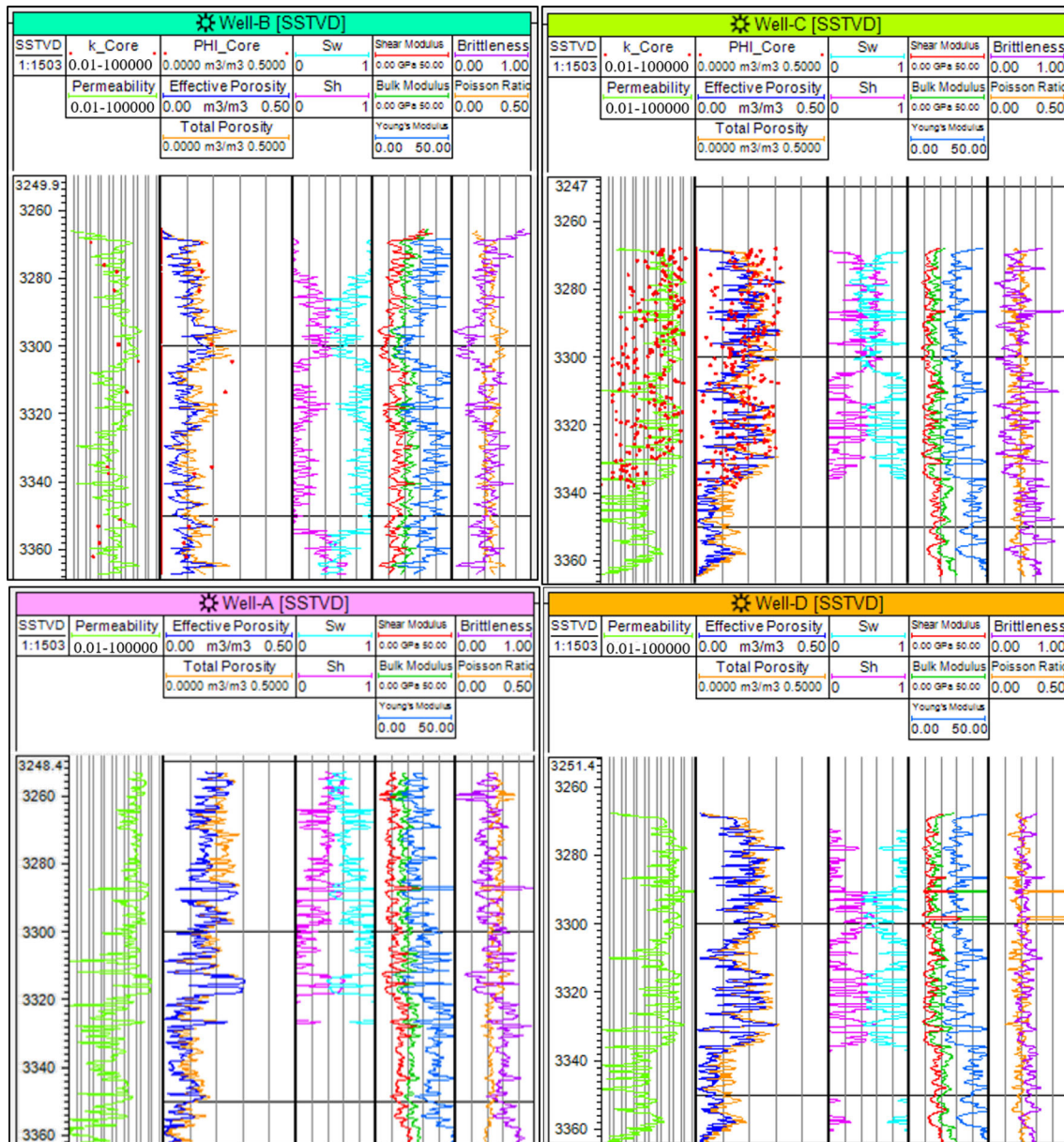


Figure 5. Interpreted log responses indicating hydrocarbon-bearing zones in C-sand interval with permeability (track 2), effective and total porosity (track 3), hydrocarbon and water saturation (track 4), geomechanical properties (track 5), Poisson's ratio, and brittleness index (track 6) in Well-A, Well-B, Well-C, and Well-D.

facies, i.e., at 3340–3364 m. The hydrocarbon saturation, permeability, and porosity were high. The elastic moduli were relatively consistent but high at the bottom of the reservoir interval. Along with the sandy content, the elastic moduli were high but low in the shaley zone of 3340–3368 m (track 5). There are higher hydrocarbon saturations at the 3290–

3310 m depth; however, they considerably vary from 3310 to 3364 m because of sand–shale intercalations.

The interpretation of petrophysical analysis shows the heterogeneities and complexities in the region. Moreover, extensive characterization is significant to reduce drilling risks and to improve oil and gas recoveries.

Facies Analysis and Modeling

As earlier mentioned, the Lower Goru Formation has a variable depositional environment. The SOM methodology was used in this work to identify the electro-facies (EF) from well log data. The approach proceeded as follows: the combination of facies discrimination logs (i.e., RHOB, NPHI, GR, and photoelectric effect (PEF)) was employed to identify the ‘k’ clusters of well log responses with similar characteristics (Fig. 6). Each cluster was labeled with a specific ‘EF’ identification. Four EF

were identified in the target interval and classified into four lithofacies based on field reports, core data, and pattern recognition and classification of gamma-ray log response: EF4 = shale lithofacies, EF3 = sandstone with subordinate shale, EF2 = shaley sandstone lithofacies, and EF1 = sandstone lithofacies (hydrocarbon effect). A complete description of lithology, facies element, and ranges of reservoir properties based on EF in the target interval is summarized in Table 2.

To evaluate the performance of identified EF with measured laboratory data, the confusion matrix

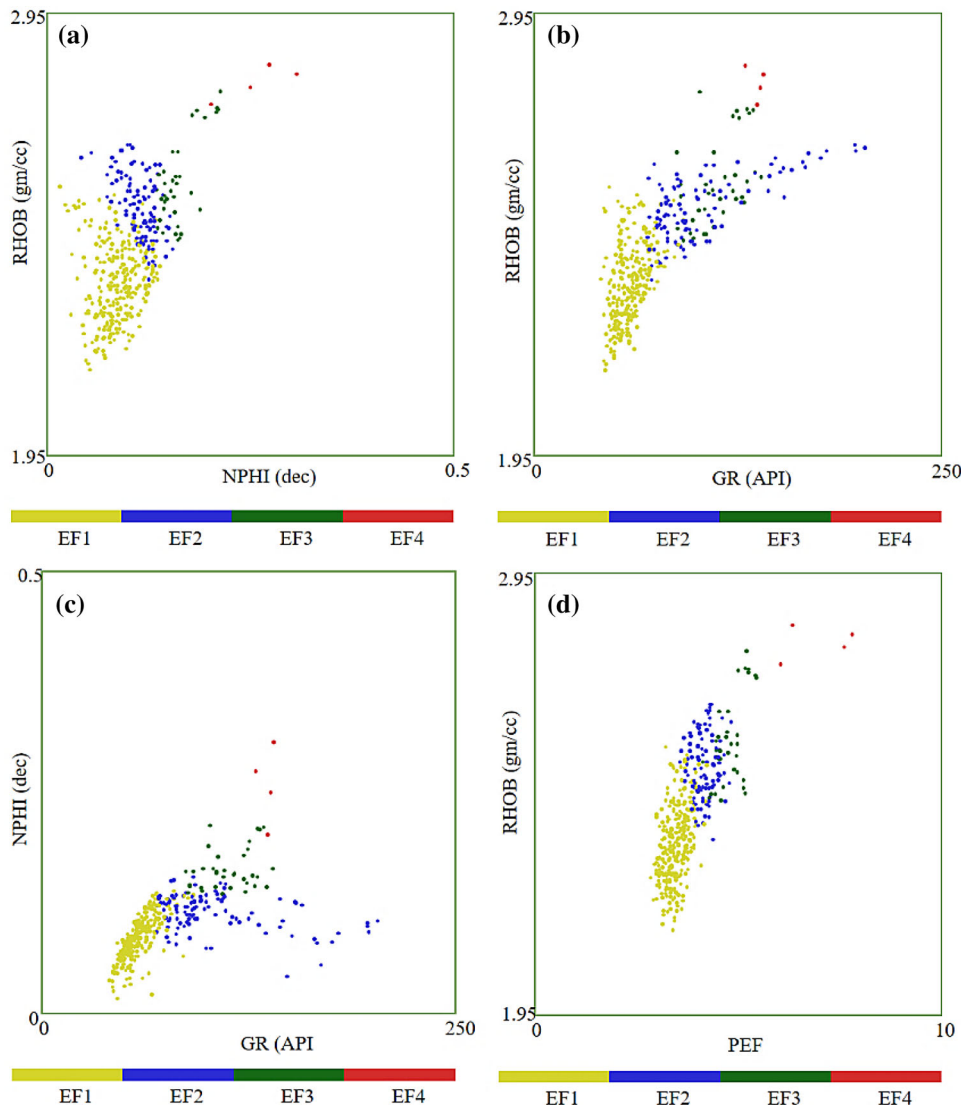


Figure 6. Plot of SOM clustering and discrimination of four electro-facies (EF) in (a) NPHI vs. RHOB, (b) GR vs. RHOB, (c) GR vs. NPHI, and (d) PEF vs. RHOB cross-plots.

Table 2. Descriptions of lithology, facies element, and ranges of reservoir properties based on electro-facies (EF) of Well-C

Depth (m) interval	Lithofacies	Deposition environment	EF coding	POR (Dec)	Clay (Dec)	GR (API)
3268–3305 Z-1	Coarse-grained sand	Deltaic distributary channel	EF1	0.14–0.33	0.00–0.10	0–60
3305–3310 Z-2	Sandstone with subordinate shale	Shore face	EF2	0.12–0.21	0.10–0.30	60–100
3310–3339 Z-3	Coarse-grained sand	Deltaic distributary channel	EF1	0.16–0.31	0.00–0.20	0–60
3339–3351 Z-4	Sand-shale intercalation	Outer shelf	EF3	0.02–0.14	0.10–0.40	55+
3351–3359 Z-5	Shale	Tidal	EF4	0.02–0.12	0.10–0.30	60–100

POR porosity, Clay clay mineralogy

Table 3. Performance of SOM facies analysis from confusion matrix

Predicted	True EF1	True EF2	True EF3	True EF4
EF1	43	0	0	9
EF2	0	0	27	26
EF3	53	0	82	161
EF4	0	0	4	332
Total	96	0	113	528

The last row (in red) indicates the total number of electro-facies (EF), and the values in the diagonal (in green) are the number of electro-facies (EF) classified correctly by the SOM

for each distinct EF class zone was developed, as summarized in Table 3. It is shown that the predicted EF retains a reasonably good correlation with the interpretation of core data, signature analysis, and published data (Berger et al. 2009; Du et al. 2019). It should be noted, however, that the resolution of the log scale was considerably less than the interpretation of core data for identifying thin shale layers. The classification performances for each EF class zone from the confusion matrix exhibit an accuracy of approximately 62%. Among all four EFs, it should be noted that EF4 achieves the best classification results against core data and signature analysis.

The lateral distribution of lithofacies identified from SOM clustering was further performed using the Gaussian-indicating algorithm to spread spatially discrete data. To display the lateral and vertical distributions of facies in the study area, Figure 7 shows the cross-sectional analysis passing through five wells. In cross sections 1 and 2, the vertical proportion curves exhibit a thicker and higher proportion of shaley sandstone and sandstone lithofa-

cies; however, these gradually convert to shale lithofacies along zones 3–5. In cross section 3, the proportion of shaley sandstone was higher than sandstone lithofacies. Gradually, however, they change to shale and sandstone lithofacies. In cross section 4, the facies proportion exhibits equal amounts of sandstone, shaley sandstone, and shale lithofacies. These vary from the lithofacies of complex depositional setting in the marginal marine to that of the shallow marine environment.

A 3D facies distribution map across the study area reveals a high percentage of shaley sandstone and sandstone facies with a significant amount of shale (Fig. 7b).

The reliability of models based on the Gaussian-indicating simulation algorithm was verified by investigating the goodness of fit among different facies trends from SOM clustering, up-scaled, and modeled facies. From the cumulative data analysis of facies modeling, the estimated and up-scaled facies information shows good agreement.

Seismic Inversion

The prior steps adopted in this work for seismic inversion involve well–seismic ties, wavelet extractions, and generation of synthetic seismograms. The wavelet estimated from the measured sonic and density log was convolved with the reflectivity series to generate a synthetic seismogram for correlation with seismic traces (Fig. 8). The extracted wavelet that covers the target horizons within a specified time window (2100–2400 ms) was used in the AI inversion. The MLC + PSO and BP neural network inversion algorithms were employed for the seismic

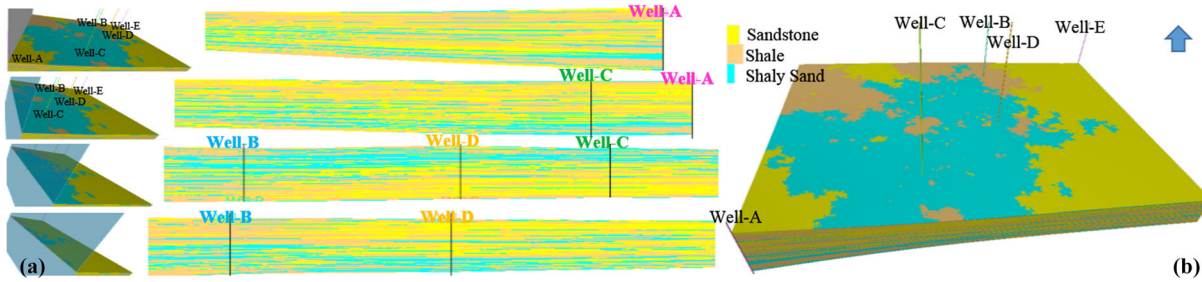


Figure 7. (a) cross-sectional analysis of facies distribution; (b) 3D facies model of study area.

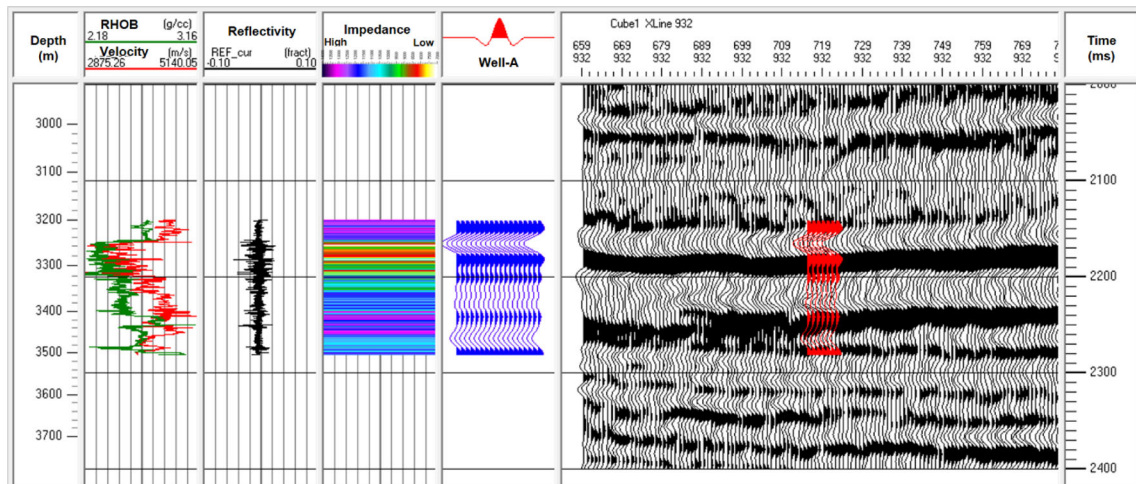


Figure 8. Generation of synthetic seismogram using data of Well-A. The synthetic and extracted seismic traces at the well location are shown in blue and red, respectively.

data of the Sawan area. The obtained results from both methods are discussed as follows.

MLC + PSO Inversion Strategy

Figure 9 shows the results when the MLC + PSO inversion strategy was applied to the interpreted 3D seismic volume. It has been demonstrated that the MLC + PSO inversion strategy can efficiently capture the lateral variations in AI with a high resolution (arrow). The combination of MLC and PSO can establish not only the nonlinear projection relationship between the log-derived AI and seismic waveform, but also calculate the appropriate weights to achieve a more stable prediction. The zone of interest, i.e., the C-sand interval, was in the

range 2100–2250 ms. The AIs vary from 7000 to 7500 (g/cc) × (m/s), from 8500 to 9500 (g/cc) × (m/s), and from 10,500 to 13,500 (g/cc) × (m/s), corresponding to sandstone, sandstone with subordinate shale, and shale lithofacies, respectively. Note that the variation in AI is associated with the changes in facies distribution, i.e., the time interval with low AI (7500–8500 (m/s) × (g/cc)), corresponding to sand layers and indicating a possible gas-saturated zone (shown with arrow) (Ali et al. 2018). The overlying stratum with high impedance values (10,500–13,500 (m/s) × (g/cc)) that exceed 2100 ms is probably a good sealing unit for a potential reservoir. It should be noted that the thin shale layers and sand–shale intercalation present within the reservoir interval are better resolved by the MLC + PSO inversion strategy (shown with arrow). Although a complex

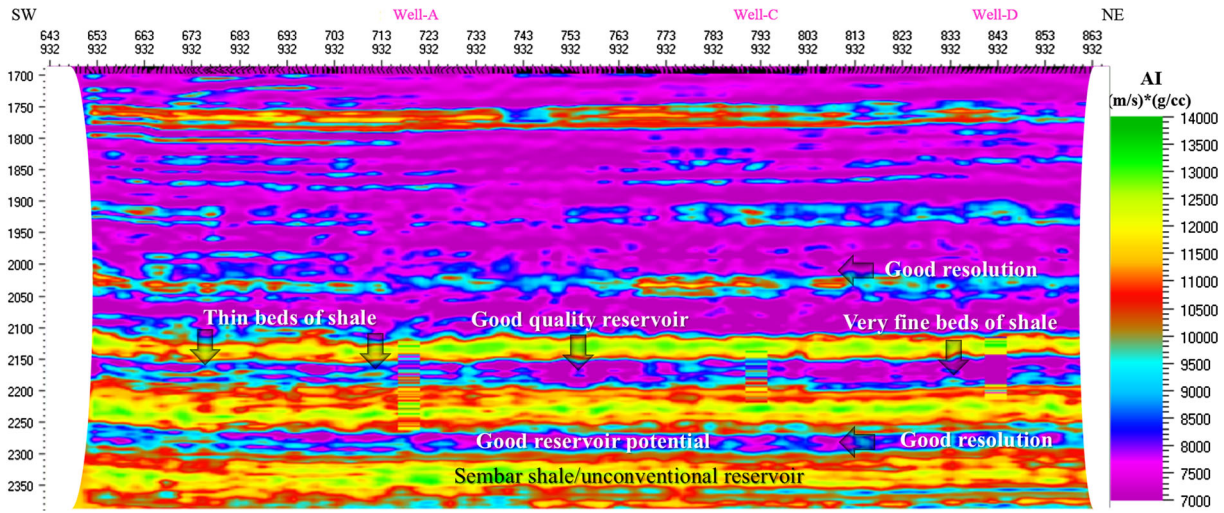


Figure 9. Inverted AI for inline 932 using MLC + PSO inversion. The impedance logs of Well-A, Well-C, and Well-D exhibit good matching and high resolution with the inverted impedance surface (2100–2250 ms).

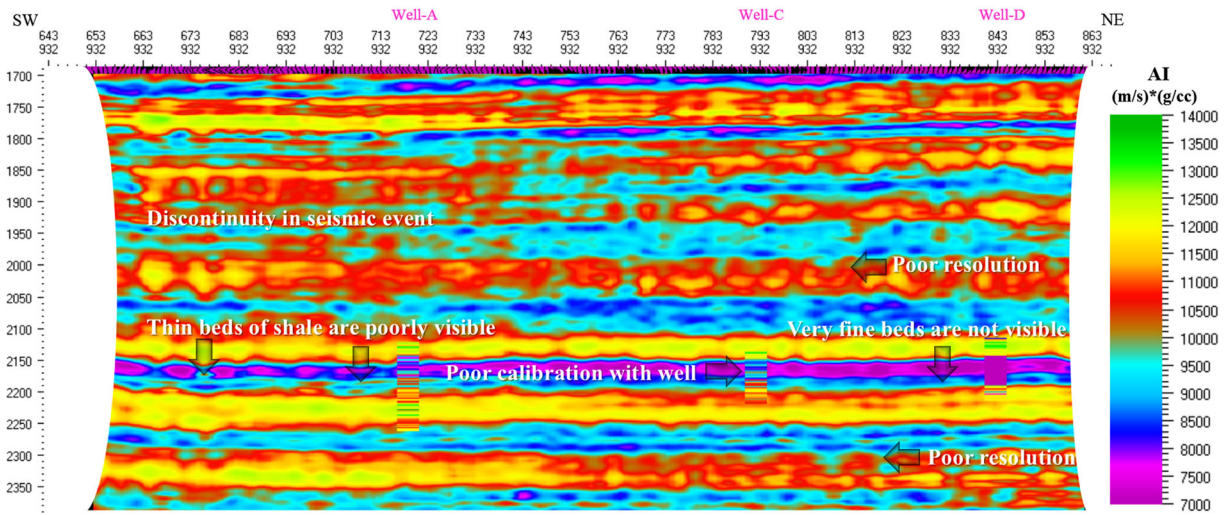


Figure 10. Inverted AI for inline 932 using BP neural network seismic inversion. The impedance logs of Well-A, Well-C, and Well-D do not agree well with the inverted impedance surface (2100–2250 ms).

and nonlinear relationship exists between the thinly layered media and seismic waveforms, the MLC establishes a nonlinear projection relationship to capture the thinly layered media from the seismic waveform. The facies probability analysis exhibits good correlation between sandstone and shale lithofacies with low and high AIs. The AI significantly varies depending on the lithology variation in

each zone. The MLC + PSO inversion strategy was used to constrain the spatial distribution of reservoir parameters because it has a good calibration.

Furthermore, the zone between 2250 and 2300 ms has a low impedance (7000–9000 (m/s) (g/cc)), indicating a possible gas-saturated but unexplored zone. A favorable distribution of medium and high impedance layers was less than 2300 ms;

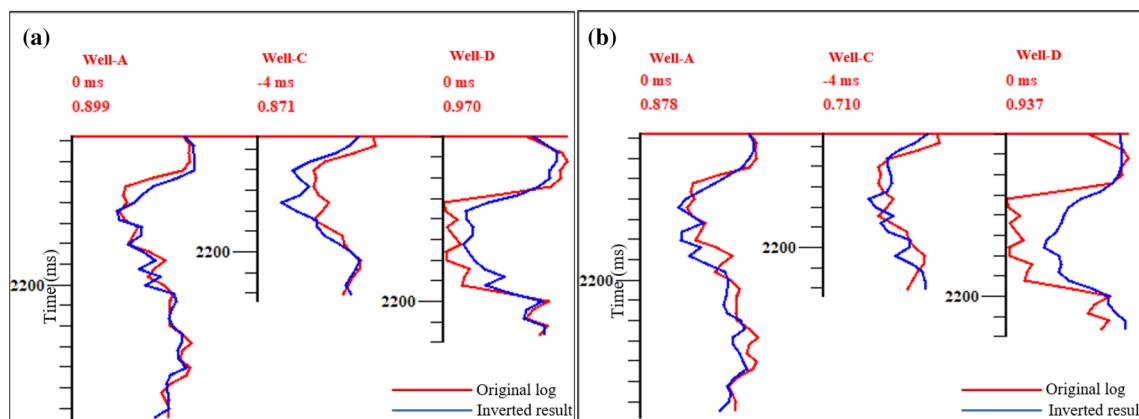


Figure 11. Analysis plots for comparison of original logs (blue) and inverted results (red) at Well-A, Well-C, and Well-D; (a) MLC + PSO inversion method; (b) BP neural network seismic inversion.

these layers are probably of Sembar shales, which could be considered as an unconventional perspective that requires further investigation with other factors, such as the TOC.

BP Neural Network Seismic Inversion

To illustrate the benefits of the proposed strategy, the inverted AI was estimated on a 3D seismic cube using the BP neural network, as shown in Figure 10. According to the inverted AI profile, the lateral and vertical AI variations from the BP neural network exhibit low resolution and inadequate performance in the discontinuity of the seismic event and the unclear boundary of the inverted AI. Unfortunately, the random weights in the BP neural network initialization have led to the convergence of the local minimum and extreme randomness. Furthermore, the selection, crossover, and mutation operators generated by the BP neural network are inefficient to optimize the inversion results. The inverted AI from the BP neural network was not sufficient to capture the small lithological variations, i.e., thin shale beds (arrow), because of random weights. The overall lateral and vertical variation resolutions of impedance estimated by the BP neural network were inadequate, thus resulting in the discontinuity of seismic event (arrows).

The post-stack seismic inversion analysis plot for Well-A, Well-C, and Well-D indicate a reasonably good agreement between the inverted (red line) and computed AIs (blue line) within the calculation window (Fig. 11). The overall correlation coeffi-

cients between the inverted and computed values are 0.90, 0.87, and 0.97 in Well-A, Well-C, and Well-D, respectively. These high correlation coefficients show that the calibration between inverted seismic data and well log AI verifies the reliability and accuracy of the proposed approach.

The application of the MLC + PSO to a 3D seismic cube provides a reasonably good estimation of AI and it may be linked to the provision of further information for detailed reservoir characterization. As an optimized method, the BP neural network seismic inversion algorithm captures the lithological variations in the best possible approach. It has, however, yielded low resolutions and failed to capture thin shale layers because of inefficient selection, crossover, and mutation operators. In contrast, the MLC + PSO method was more capable of capturing the thin shale beds and sand–shale intercalation within and below the reservoir interval because of its nonlinear projection relationship with appropriate weights. Moreover, the spatial variations of AI in the MLC + PSO inversion strategy provide high resolution and good agreement with well data compared with the BP neural network seismic inversion algorithm.

ESTIMATION OF RESERVOIR PARAMETERS

To establish the relationship between AI, porosity, permeability, and hydrocarbon saturation, a cross-plotting between porosity, permeability, and AI with hydrocarbon saturation (Sat. HC) was

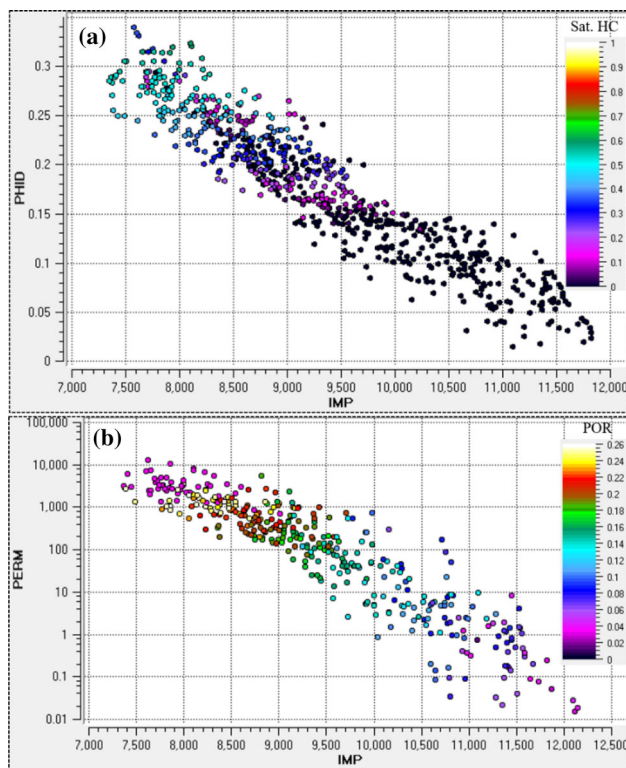


Figure 12. Cross-plots of impedance (AI) (a) vs. porosity (PHID) with a color bar representing hydrocarbon saturation (Sat. HC) and (b) vs. permeability (PERM) with a color bar representing PHID.

generated as a third parameter (Fig. 12a and b). Ali et al. (2018) reported that the AI and log porosity assume a linear approximation. A linear regression analysis was therefore employed in this study, and a best fit regression was achieved. Figure 12 shows the increase in porosity, permeability, and hydrocarbon saturation with the decrease in AI. It was observed that a linear relationship between porosity, permeability, and hydrocarbon saturation vs. AI has a negative slope. The regression equations obtained from these cross-plots are used to transform the AI inversion into reservoir parameters.

Seismic Porosity vs. Well Porosity

The inverted porosity models exhibit a good reservoir porosity of up to 24% along with the low impedance values of Well-A, Well-C, and Well-D at 2150–2170 ms (Z-1 and Z-3). The porosity varies from a minimum of 14% (Well-A) to a maximum of 24% (Well-C and Well-D) with an average of 18% (Fig. 13). The dominant lithology in this zone

was sandstone (Table 2). The porosity increases along the NE to SW direction, and a highly porous reservoir exists between Well-A, Well-C, and Well-D (shown with arrow). The shale distribution in the reservoir interval was one of the factors that control the reservoir potential. It was shown that porosity drastically decreased (< 0.10) at the bottom (2170–2220 ms) when shale and sandy shale facies were predominant (Table 2, Z-5), corresponding to high AI values (10,500–14,000 (m/s) \times (g/cc)).

The zone below 2250 ms also has a low impedance (7000–9000 (m/s) \times (g/cc)) and good porosity values ($> 10\%$). The low impedance and higher porosity in this zone could potentially form the best reservoir (marked with arrow).

It was observed that the zone below 2300 ms has a good porosity range with medium-to-high impedance layers characterized by shale and shaley sand facies. This zone could be further investigated as unconventional play with other considerable factors, such as permeability, saturation, and elastic parameters (shown with white circles).

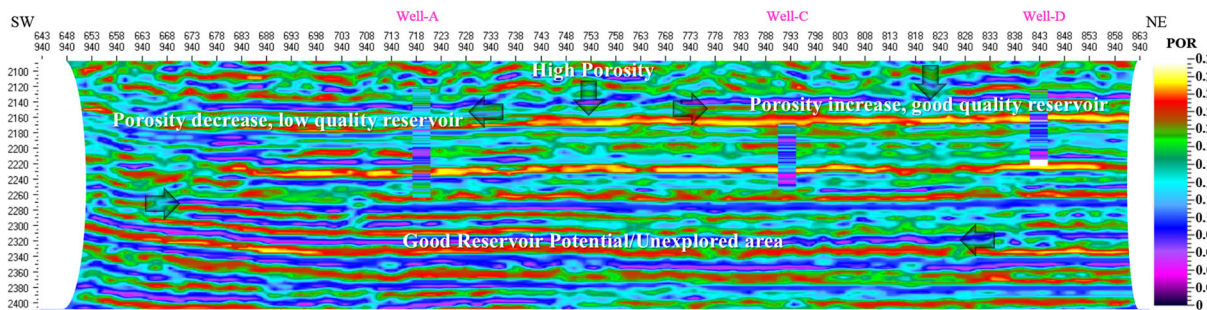


Figure 13. Seismic porosity obtained by MLC + PSO inversion in C-sand interval at 2100–2250 ms.

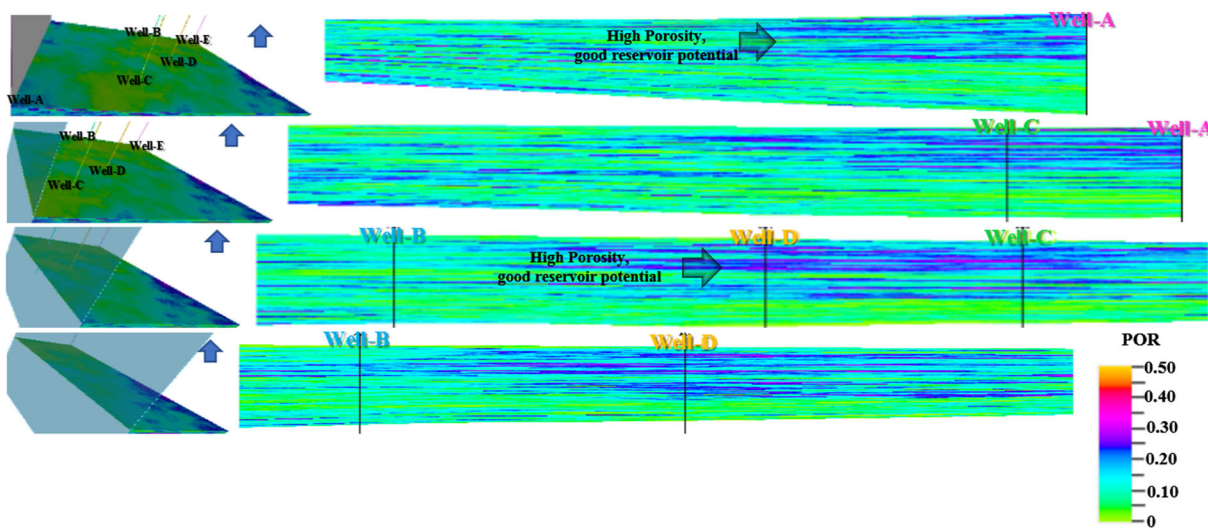


Figure 14. Porosity model populated from porosity logs using SGS algorithm in C-sand interval at 3260–3360 m.

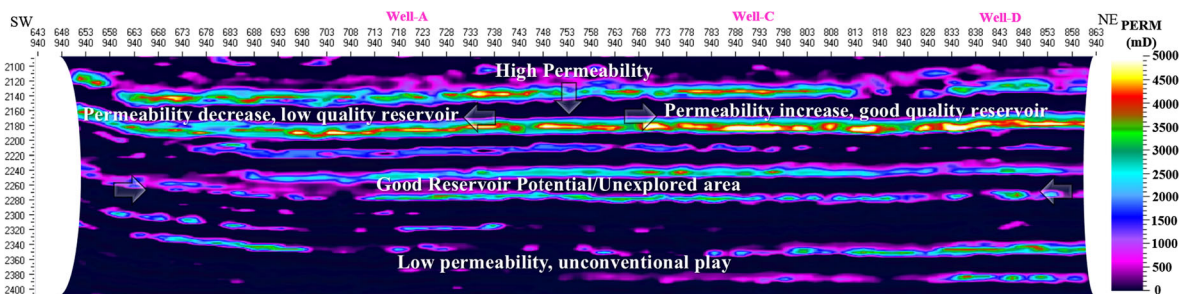
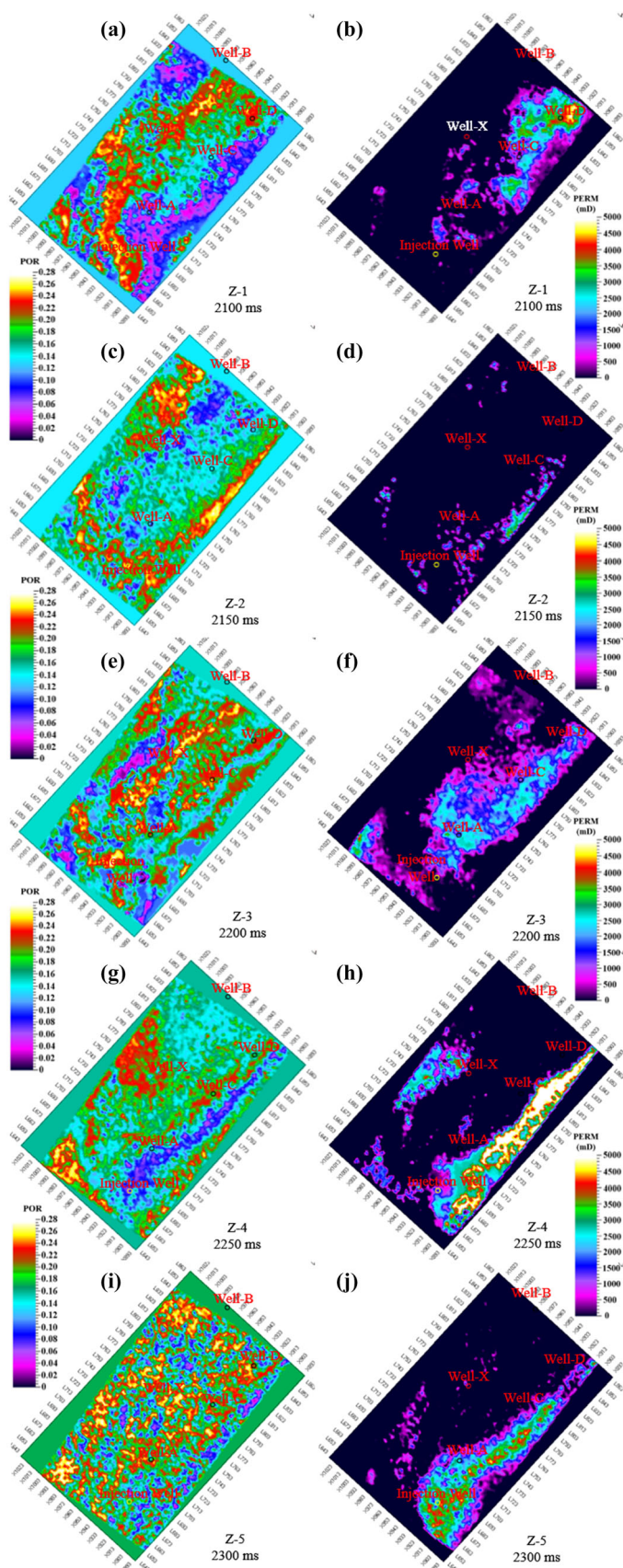


Figure 15. Inverted permeability map of seismic section of Sawan area. The MLC + PSO inversion provides insight on the spatial variability of seismic permeability.



◀ **Figure 16.** Time slices of porosity and permeability at various intervals using MLC + PSO inversion method. (a and b) at 2100 ms; (c and d) at 2150 ms; (e and f) at 2200 ms; (g and h) at 2250 ms; (i and j) at 2300 ms.

To ensure the reliability of MLC + PSO inversion results, the inverted porosity from seismic inversion was compared with the porosity model computed from porosity logs using the sequential Gaussian simulation (SGS) algorithm (Fig. 14). Note that the comparison indicates a uniformity between the two porosity models as constrained by the MLC + PSO inversion and SGS algorithm (shown with arrow). Nevertheless, the porosity model constrained by MLC + PSO inversion provides insight on the spatial distribution of porosity values (0.04–0.24) within the Sawan area.

Inverted Permeability Model

The inverted permeability models also exhibit good reservoir permeability, low impedance, and high porosity values laterally and vertically around Well-A, Well-C, and Well-D (Fig. 15). A significant inverse correlation obtained from the cross-plotting of AI and permeability logs suggests that the AI inversion is the key to predict permeability (Fig. 12).

The higher permeability sandstone facies observed at 2150–2170 ms (Z-1 and Z-3) was correlated with low AI values (7500–9500 (m/s) × (g/cc)). On the other hand, the lower permeability shaley sand facies observed at 2170–2220 ms corresponds to high AI values (10,500–14,000 (m/s) × (g/cc)). This implies that the higher permeability in the reservoir interval potentially forms the best reservoir laterally from NE to SW (Fig. 15).

The zone below 2250 ms also has a low impedance (7000–9000 (m/s) × (g/cc)) and good porosity values (> 20%). These low impedance and high porosity values at this particular zone indicate a gas-saturated anomaly, which can be considered as the best reservoir (marked with an arrow). Moreover, the zone below 2300 ms exhibits low permeability and a porosity that is less than 20% with a medium-to-high impedance. This implies that this zone should be investigated further for unconventional play (shown with white circle).

Integrated Petrophysical Data Interpretation

To comprehend the spatial changes in the reservoir interval, time slices of porosity and permeability at a 50-ms time interval are generated using the MLC + PSO inversion method, as shown in Figure 16. According to the time slices of inversion results, Z-1 and Z-3 exhibit high porosity and permeability, thus significantly boosting the credence to delineate the potential reservoir. The porosity and permeability of Z-1 and Z-3 are attributed to sandstone lithofacies (EF1) of coarse-grained sand deposits at the deltaic distributary channel (Table 2). The laboratory-measured porosity and permeability data in Well-C and Well-B also support the inverted results, i.e., the upper zone (3200–3260 m) has high porosity and permeability (Table 1). Compared with Z-1 and Z-3, Z-2 exhibits a lower porosity and permeability. This zone was characterized by a medium-to-high impedance and it corresponds to sandstone with subordinate shale, i.e., EF2 (Table 2). The measured data in Well-C and Well-B also indicate low porosity and permeability (Table 1). Zones Z-4 and Z-5 also exhibit a relatively good porosity and permeability; however, there was no well control up to these particular zones.

Accordingly, the MLC + PSO inversion strategy has achieved good contrast in the lateral trend of porosity and permeability at various time intervals that can be directly utilized to define the threshold in each potential zone.

Inverted Hydrocarbon Saturation Model

Porosity and hydrocarbon saturation are directly correlated because of their linear and positive trends. In view of this, the direct estimation of hydrocarbon saturation from seismic inversion can be implemented using AI, porosity, and hydrocarbon saturation cross-plots (Fig. 12). The spatial distribution of inverted hydrocarbon accumulation in the Sawan area is shown in Figure 17.

An inversion profile in the (2150–2170)-ms time interval (Z-1 and Z-3) also delineates the good potential of hydrocarbon saturation and low impedance (7500–9500 (m/s) × (g/cc)) and highly porous and permeable layers. The hydrocarbon saturation varies from NE (Well-C and Well-D) to SW (Well-A), and an average saturation of approximately 45% was identified in the study area.

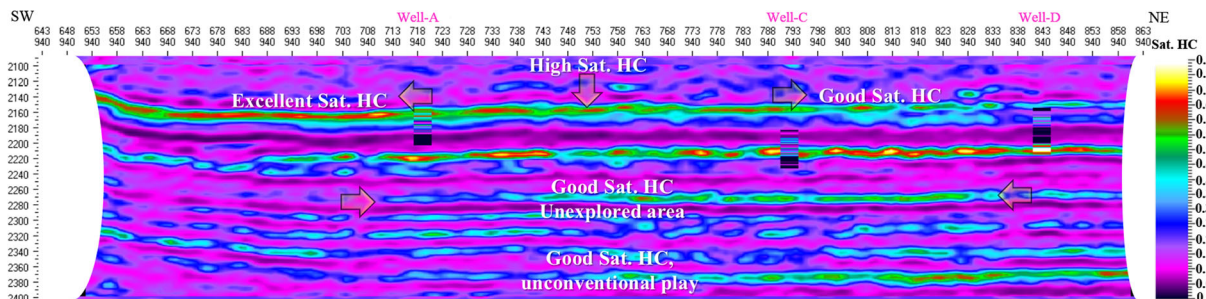


Figure 17. Inverted HC saturation map for seismic section of Sawan area. The MLC + PSO inversion exhibits a good calibration of the spatial variability of saturated HC from the inversion profile and well logs.

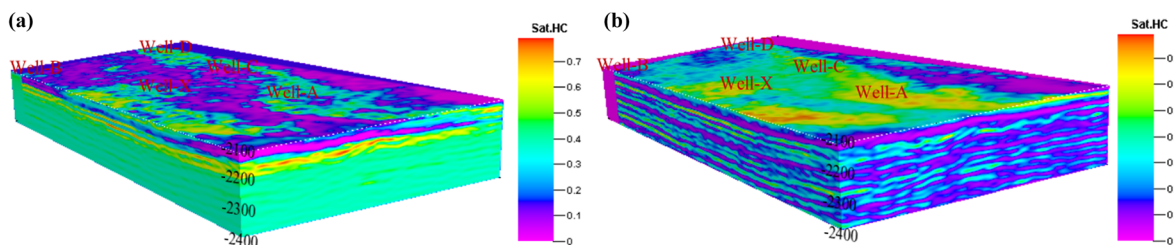


Figure 18. Hydrocarbon saturation model obtained by (a) BP neural network-based inversion and (b) MLC + PSO inversion strategy at 2150 ms.

At the bottom of the reservoir interval (Z-5), the low hydrocarbon saturation and high impedance (10,500–14,000 (m/s) × (g/cc)) are caused by the change in sand–shale facies present in this zone. The calibrations of hydrocarbon saturation from the well logs and inversion profile exhibit good agreement.

It should be noted that a good anomaly of hydrocarbon saturation exists below the 2260-ms interval, and further investigation was necessary to explore the potential zone (indicated by arrows). The summary of inverted petrophysical parameter analysis shows that zones 1, 3, and 4 potentially form the best reservoir laterally and vertically from NE to SW.

Figure 18 shows the 3D models of hydrocarbon saturation obtained by the BP neural network inversion (Fig. 18a) and MLC + PSO inversion (Fig. 18b). It should be noted that the MLC + PSO inversion was more capable than the BP neural network inversion in predicting vertically and horizontally the hydrocarbon saturation to build a high-resolution 3D model in a complete seismic volume. It is notable that the MLC + PSO inversion successfully captures the variations in vertical saturation

because of the alternate sand and shaly sand layers.

Figure 19 briefly explains the values in the histogram of corresponding petrophysical properties. As previously mentioned, the dominant lithology in the target interval was sandstone and shaly sandstone with intercalations of shale. As a result, good-to-excellent total and effective porosities were developed in the study area with average values of 14% and 11%, respectively. The estimated permeability was in the range 0.001–1000 mD. The hydrocarbon saturation reaches a high of 80% in the range 0.08–0.8 (with an average of 0.60).

Inverted Models of Young’s Modulus and Poisson’s Ratio

Figure 20 shows significant variations in Young’s modulus and Poisson’s ratio in the range 22–46 MPa and 0.20–0.25, respectively. These variations are expected because of abrupt changes in lithology, porosity, permeability, and fluid content in the reservoir interval. The examination of variations in Young’s modulus and Poisson’s ratio with low AI

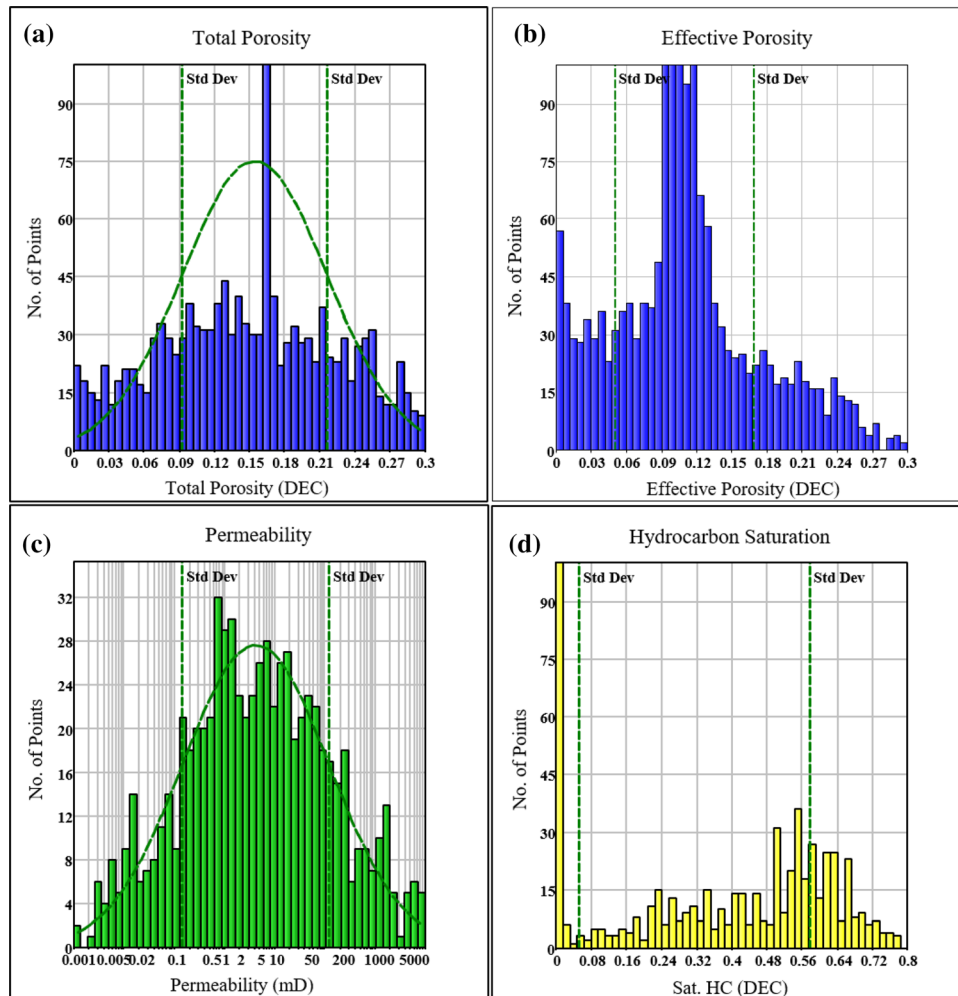


Figure 19. Histogram analysis of petrophysical properties of reservoir interval: (a) total porosity; (b) effective porosity; (c) permeability; (d) hydrocarbon saturation.

(7500–9500 (m/s) × (g/cc)), high porosity (> 20%), permeability (> 1000 mD), and saturation (> 60%) can aid in identifying the suitable areas for drilling wells. The analysis of Young’s modulus and Poisson’s ratio with petrophysical properties could be effective in drilling inclined wells and avoiding areas with potential wellbore stability problems.

It is noteworthy that the areas where Poisson’s ratio was low and Young’s modulus was high are confined below 2300 ms. More importantly, the petrophysical properties (i.e., permeability < 1 mD, porosity < 10%, and hydrocarbon saturation > 40%) s also confined below 2300 ms (marked with a box). The summary of inverted reservoir parameter analysis thus confirms that the zone be-

low 2300 ms potentially forms the best reservoir for the unconventional perspective.

Figure 21 presents the 3D models of dynamic Young’s modulus and Poisson’s ratio obtained by the MLC + PSO inversion. It can be observed that the MLC + PSO inversion was the most appropriate for predicting dynamic Young’s modulus and Poisson’s ratio laterally and vertically to estimate a refined 3D model in the complete seismic volume.

Integrated Model Interpretation

Petrophysical and geomechanical parameters are extremely important in reservoir characteriza-

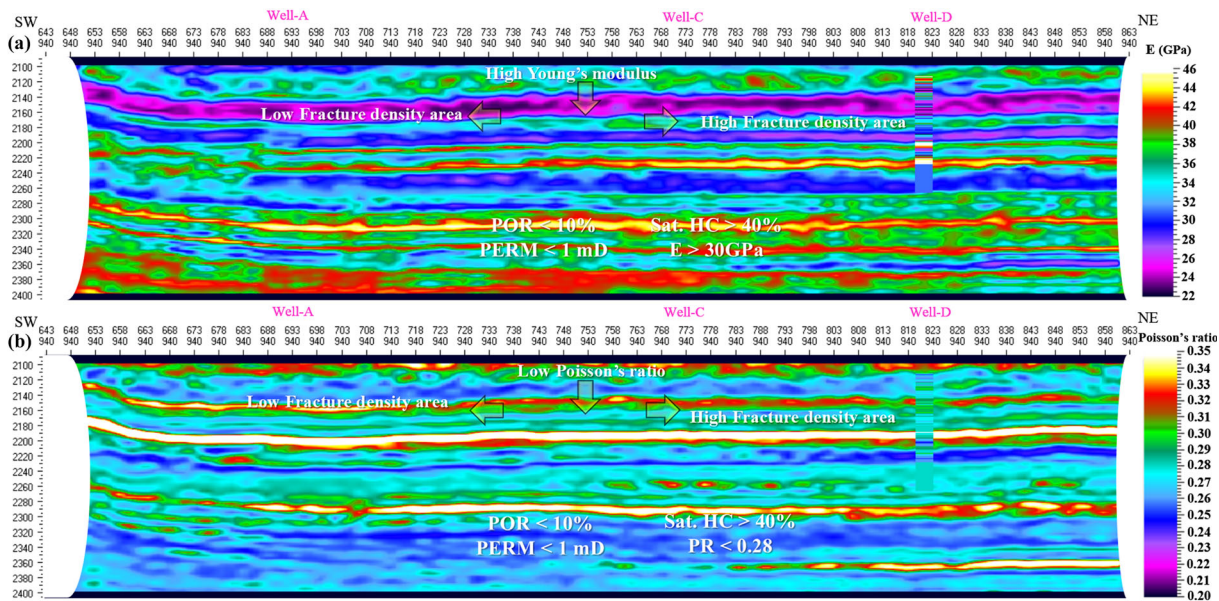


Figure 20. (a) inverted dynamic Young's modulus; (b) inverted dynamic Poisson's ratio for seismic section of Sawan area. The areas shown with arrows indicate locations with high fracture density and low risk of borehole failure. This information is essential for drilling.

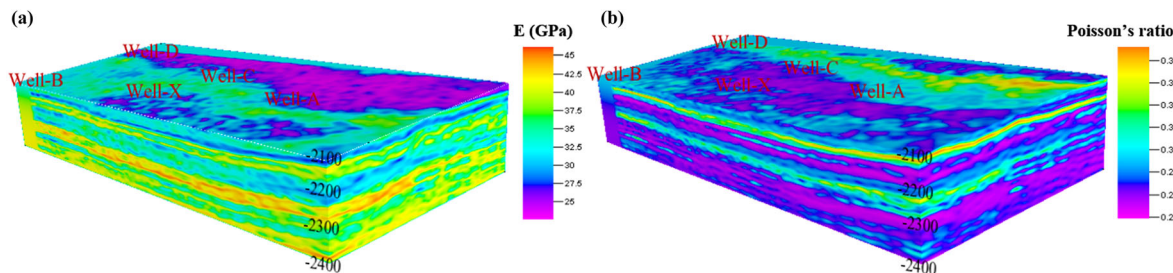


Figure 21. 3D models of (a) dynamic Young's modulus and (b) Poisson's ratio obtained from MLC + PSO inversion at 2150 ms.

tion; however, the quantitative estimation of these parameters is equally difficult. In the evaluation of these reservoir properties, more problems could arise if the intercalated shale is trapped in the sedimentary column of the reservoir interval. Traditionally, the petrophysical and geomechanical parameters are determined by log data, numerical models, and rock core laboratory procedures. Log and laboratory-measured core data provide accurate information at certain locations around the drilling well. A degree of uncertainty therefore exists when the spatial distribution of reservoir parameters in a region is estimated by only using well log data. To

achieve the anticipated result from the spatial distribution of detailed reservoir characterization, the integration of multiple datasets (3D seismic, well logs, and cores) is a reliable approach.

In this study, the proposed strategy (MLC + PSO) applied to a 3D seismic cube provides a reasonable estimate of AI and spatial variations of petrophysical and geomechanical parameters to identify hydrocarbon-bearing zones. It is noteworthy that the proposed strategy captures the lateral and vertical variations in AI with high resolution and varies with an abrupt change in extremely thin sand/shale layers (i.e., the low AI, which corresponds to

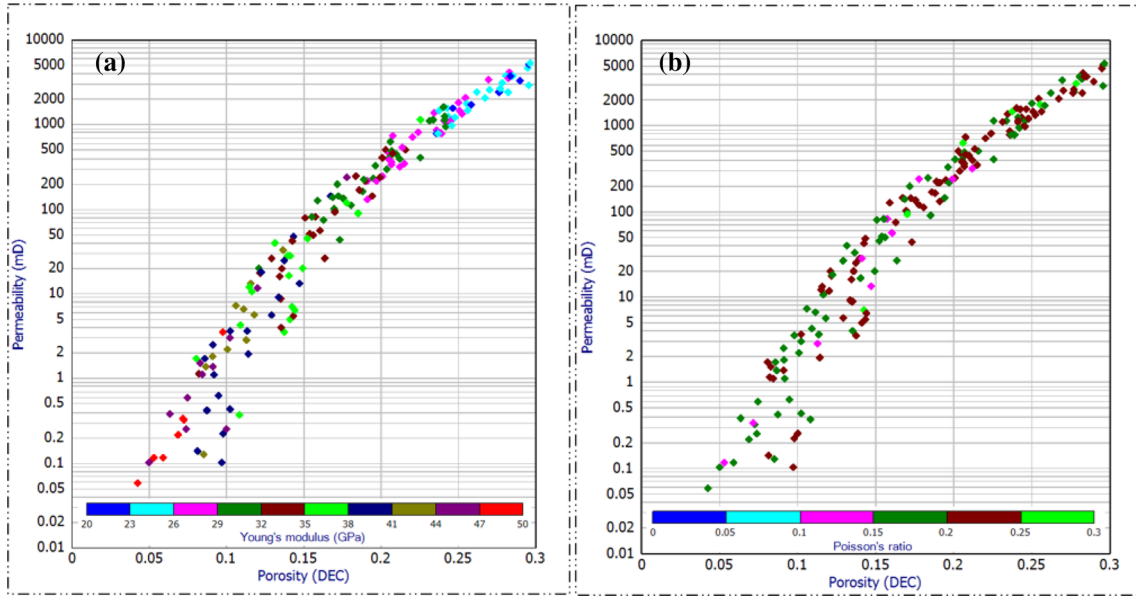


Figure 22. Relationships between petrophysical and geomechanical properties: (a) porosity and permeability with Young's modulus; (b) porosity and permeability with Poisson's ratio.

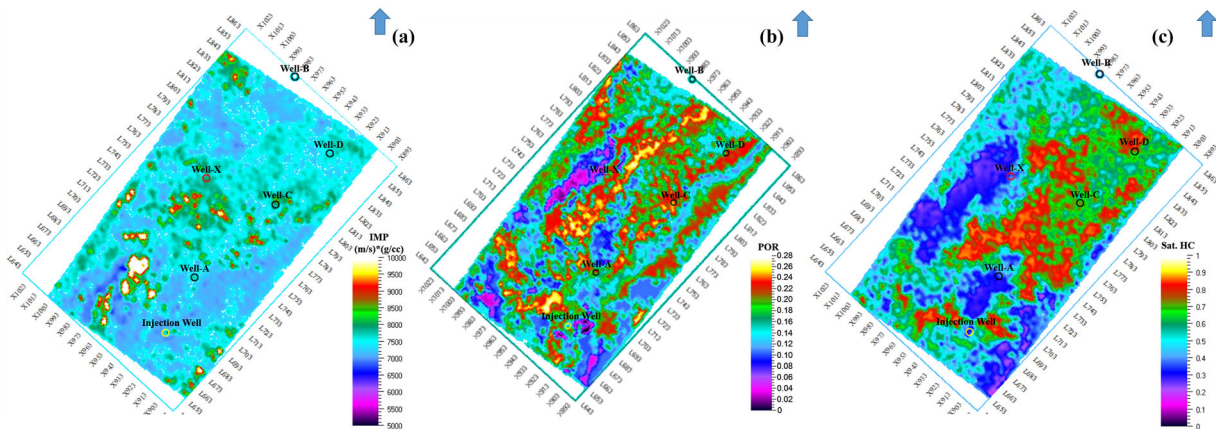


Figure 23. Time slices of (a) acoustic impedance (AI), (b) porosity, and (c) hydrocarbon saturation (Sat. HC).

sand layers, indicates a possible gas-saturated zone). The spatial variability of inverted porosity and permeability profiles affords a good agreement between well and core data. On the other hand, the lateral

and vertical variations of AI obtained through the BP neural network were unable to capture the abrupt changes in lithology and thin sand/shale layers.

Table 4. Production data of studied wells (Ashraf et al. 2018)

Well ID	Production (m ³)
Well-A	361,860.94
Well-C	692,266.27
Well-D	389,945.30
Well-X	133,278.54

Figure 22 shows the cross-plot of porosity vs. permeability overlaid with fundamental elastic moduli (Young's modulus, Poisson's ratio). Such plots highlight the porosity and permeability variations with elastic moduli, e.g., the increase in porosity and permeability tends to decrease Young's modulus (Fig. 22a). Poisson's ratio, however, does not exhibit any distinct relationship with porosity and permeability (Fig. 22b).

Based on the integration of multiple datasets (petrophysics, geomechanics, and post-stack seismic inversion), the study area was evaluated in the location of better reservoir zones. Figure 23 shows the inverted AI (IMP), porosity (POR), and hydrocarbon saturation (Sat. HC) slices estimated from the MLC + PSO inversion strategy along with the target interval. The time slices of inverted porosity and hydrocarbon saturation show that the area around NE of Well-A has a high porosity (~ 26%) and a hydrocarbon saturation that exceeds 75% (Fig. 23b and c, respectively). Moreover, the area that lies between Well-A and Well-C has good properties for oil and gas production [i.e., hydrocarbon saturation was approximately 75%, porosity was 24%, and Well-A and Well-C have gas production values of 361,860.94 and 692,266.27 m³, respectively (Table 4)]. The area adjacent to Well-D and injection well also has a good porosity and a high hydrocarbon saturation. The hydrocarbon saturation in the region varies from 20% (pink color) to 80% (red color), i.e., from NE to SW. In Figure 23a, the time slices show that the low AI values follow the high porosity and high hydrocarbon saturation values in the same direction. The higher the values of porosity that low AI (IMP) values follow, the more probable that hydrocarbon-filled sand is involved.

The production data of Well-A, Well-C, and Well-D show that Well-C has the maximum production and is located in an area with high porosity and hydrocarbon saturation. On the other hand, Well-X has the minimum production and is located in an area with a relatively medium-to-low porosity and hydrocarbon saturation (Table 4).

CONCLUSIONS

In this study, the integration of MLC with PSO inversion schemes was applied to a 3D seismic cube to estimate AI. It was further linked to the spatial variation of petrophysical and geomechanical parameters for the characterization of hydrocarbon-bearing zones in a highly heterogeneous reservoir. The following conclusions are drawn.

The MLC + PSO inversion strategy was more reliable than the BP neural network inversion algorithm in discriminating between the lateral and vertical facies heterogeneity. It was also more reliable in accurately predicting the reservoir parameter distribution, i.e., low AI was more consistent with sand facies, low Young's modulus, and high porosity, permeability, and saturation. The overall correlation coefficients between the MLC + PSO inversion and measured values were 0.90, 0.87, and 0.97 in Well-A, Well-C, and Well-D, respectively, indicating that the proposed inversion strategy was reliable. To capture the geometries of thin sandstone bodies, the contrast of low and high impedance layers from the MLC + PSO inversion was more consistent than the BP neural network inversion algorithm.

The spatial distribution of inversion-based horizon slices through porosity, permeability, saturation, Poisson's ratio, and Young's modulus shows that high-potential zones are more related to hydrocarbon saturation in the range 40–80% and Poisson's ratio of 0.22–0.28. Further, these parameters are best developed in the NE to SW of the field. The hydrocarbon saturation between Well-A, Well-C, and Well-D of the reservoir was extremely high and corresponds to the area with a high potential for development wells.

The examination of variations in Young’s modulus and Poisson’s ratio along zones with low AI (7500–9500 (m/s) × (g/cc)), and high porosity (> 20%), permeability (> 1000 mD), and saturation (> 60%) can aid in identifying the suitable areas from NE to SW for well drilling and avoiding areas with potential wellbore stability problems.

The laminations along the thickness of the reservoir below 2300 ms have a permeability < 1 mD, followed by a porosity < 10%, and hydrocarbon saturation > 60% with high Young’s modulus and low Poisson’s ratio. This implies that the zone potentially forms the best reservoir for the unconventional perspective after the further investigation of other factors, such as total organic carbon content and maturity.

The methodology presented in this study provides better insights on the lateral and vertical trends of reservoir heterogeneity, which can aid in minimizing the risk and analyzing the potential zones over the entire reservoir surface by the integration of multiple datasets. Moreover, although the results obtained in this work cannot be generalized, they can be successfully applied to other basins in Pakistan with similar geological settings and anywhere in the world for reservoir characterization,

particularly for intercalated shale and variable depositional environments.

ACKNOWLEDGMENTS

This research was supported by the National Science Foundation of China (41930429 and 41774139), the research project of the China National Petroleum Corporation (2019A-33), the China National “111”. Foreign Experts Introduction Plan for Tight Oil & Gas Geology and Exploration, and the Deep-Ultradeep Oil & Gas Geophysical Exploration. We are grateful to the Beijing Rock Star Petroleum Technology Co., LTD for providing software support.

APPENDIX

Location of Sawan Gas Field

See Figure 24.

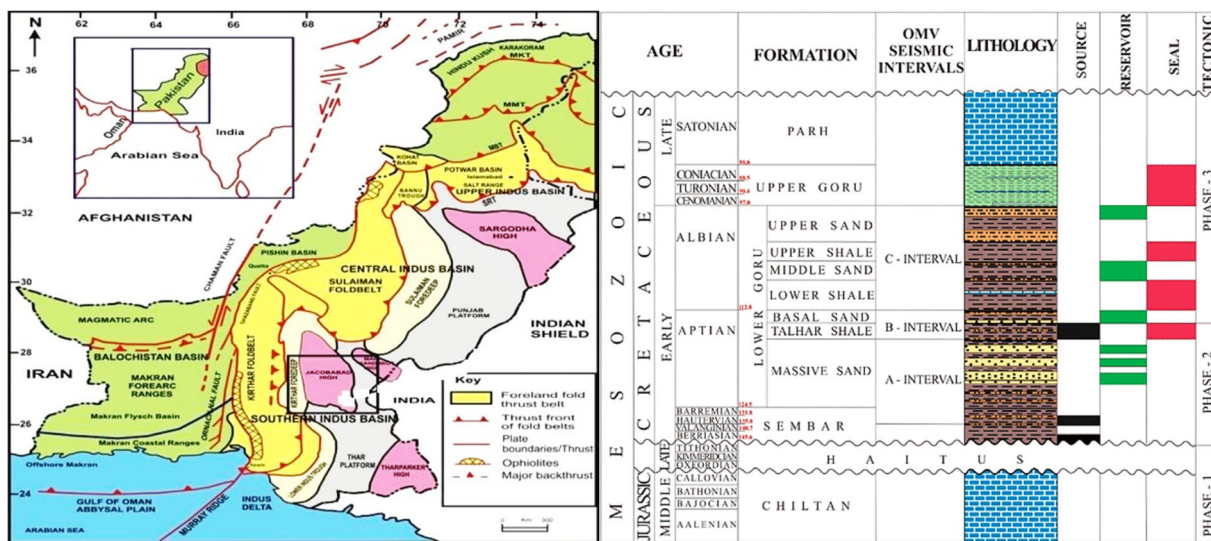


Figure 24. (a) Aerial map of structural setting and location of Sawan gas field, (b) stratigraphic column of reservoir, highlighting 'C' interval (target interval) (Yasin et al. 2019).

Estimated Permeability Model

See Figure 25.

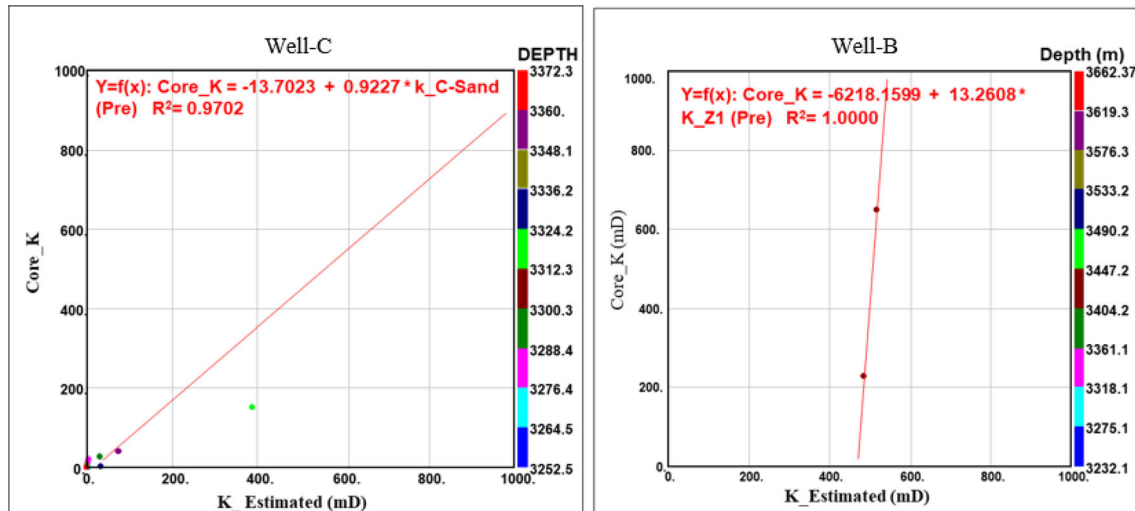


Figure 25. Regression analysis between estimated and measured permeabilities of Well-B and Well-C (Yasin et al. 2019).

REFERENCES

- Ahmad, N., Fink, P., Sturrock, S., Mahmood, T., & Ibrahim, M. (2004). Sequence stratigraphy as predictive tool in Lower Goru Fairway, Lower and Middle Indus Platform, Pakistan. In *PAPG/SPE annual technical conference, Islamabad, Pakistan* (pp. 85–104).
- Ahmed, W., Azeem, A., Abid, M. F., Rasheed, A., & Aziz, K. (2013). Mesozoic structural architecture of the middle Indus Basin, Pakistan—controls and implications. In *PAPG/SPE annual technical conference, Islamabad, Pakistan* (pp. 1–13).
- Ali, A., Alves, M., Saada, A., Ullah, M., Toqeer, M., & Hussain, M. (2018). Resource potential of gas reservoirs in South Pakistan and adjacent Indian subcontinent revealed by post-stack inversion techniques. *Journal of Natural Gas Science and Engineering*, 49, 41–55.
- Archer, S., & Rasouli, V. (2012). A log based analysis to estimate mechanical properties and in situ stresses in a shale gas well in North Perth Basin. *WIT Transactions on Engineering Sciences*, 81, 163–174.
- Ashraf, U., Zhua, P., Yasin, Q., & Anees, A. (2018). Classification of reservoir facies using well log and 3D seismic attributes for prospect evaluation and field development: A case study of Sawan gas field, Pakistan. *Journal of Petroleum Science and Engineering*, 175, 338–351.
- Aybar, U., Eshkalak, M. O., & Wood, D. A. (2015). Advances in practical shale assessment techniques. *Journal of Natural Gas Science and Engineering*, 27, 399–401.
- Berger, A., Gier, S., & Krois, P. (2009). Porosity-preserving chlorite cements in shallow-marine volcanoclastic sandstones: Evidence from Cretaceous sandstones of the Sawan gas field, Pakistan. *AAPG Bulletin*, 93, 595–615.
- Calderon, J. E. (2007). Porosity and lithologic estimation using rock physics and multi-attribute transforms in Balcon Field, Colombia. *Leading Edge*, 26, 142–150.
- Charlez, P. (1997). The impact of constitutive laws on wellbore stability: A general review. *SPE Drilling & Completion*, 12, 119–128.
- Chatterjee, R., Singha, D., Ojha, M., & Sen, M. (2016). Porosity estimation from pre-stack seismic data in gas-hydrate bearing sediments, Krishna-Godavari Basin, India. *Journal of Natural Gas Science and Engineering*, 33, 562–572.
- Das, B., & Chatterjee, R. (2018a). Well log data analysis for lithology and fluid identification in Krishna-Godavari Basin, India. *Arabian Journal of Geosciences*, 11, 231–242.
- Das, B., & Chatterjee, R. (2018b). Mapping of pore pressure, in-situ stress and brittleness in unconventional shale reservoir of Krishna-Godavari Basin. *Journal of Natural Gas Science and Engineering*, 50, 74–89.
- Demuth, H., Beale, M., & Hagan, M. (2008). *Neural network Toolbox™ 6. User's guide* (p. 907). Natick, MA: The MathWorks TM.
- Droz, L., & Bellaiche, G. (1991). Seismic facies and geologic evolution of the central portion of the Indus Fan. In M. H. Link & P. Weimer (Eds.), *Seismic facies and sedimentary processes of submarine fans and turbidite systems* (pp. 383–402). New York: Springer.
- Du, Q., Yasin, Q., Ismail, A., & Sohail, M. (2019). Combining classification and regression for improving shear wave velocity estimation from well logs data. *Journal of Petroleum Science and Engineering*. <https://doi.org/10.1016/j.petrol.2019.106260>.
- Gogoi, T., & Chatterjee, R. (2019). Estimation of petrophysical parameters using seismic inversion and neural network modeling in Upper Assam Basin, India. *Geoscience Frontiers*, 10, 1113–1124.

- Golsanami, N., Kadkhodaie-Ilkhchi, A., & Erfani, A. (2015). Synthesis of capillary pressure curves from post-stack seismic data with the use of intelligent estimators: A case study from the Iranian part of the South Pars gas field, Persian Gulf Basin. *Journal of Applied Geophysics*, *112*, 215–225.
- Golsanami, N., Sun, J., Liu, Y., Yan, W., et al. (2019). Distinguishing fractures from matrix pores based on the practical application of rock physics inversion and NMR data: A case study from an unconventional coal reservoir in China. *Journal of Natural Gas Science and Engineering*, *65*, 145–167.
- Hampson, B., Schuelke, J., & Quirein, J. (2001). Use of multi-attribute transforms to predict log properties from seismic data. *Geophysics*, *66*, 3–46.
- Khan, J. M., Moghal, M. A., & Jamil, M. A. (1999). Evolution of shelf margin and distribution of reservoir facies in Early Cretaceous of Central Indus Basin—Pakistan. In *PAPG-SPE ATC 1999* (pp. 1–23).
- Kiaei, H., Sharghi, Y., Ilkhchi, A., & Naderi, M. (2015). 3D modeling of reservoir electrofacies using integration clustering and geostatistic method in central field of Persian Gulf. *Journal of Petroleum Science and Engineering*, *135*, 152–160.
- Kumar, R., Das, B., Chatterjee, R., & Sain, K. (2016). A methodology of porosity estimation from inversion of post-stack seismic data. *Journal of Natural Gas Science and Engineering*, *28*, 356–364.
- Leiphart, D. J., & Hart, B. S. (2001). Comparison of linear regression and a probabilistic neural network to predict porosity from 3-D seismic attributes in Lower Brushy Canyon channeled sandstones, southeast New Mexico. *Geophysics*, *66*, 1349–1358.
- Mavko, G., Mukerji, T., & Dvorkin, J. (2009). *The rock physics handbook: Tools for seismic analysis of porous media*. Cambridge: Cambridge University Press.
- Milan, G., & Rodgers, M. (1993). Stratigraphic evolution and play possibilities in the Middle Indus Area, Pakistan. In *SPE Pakistan seminar*, Islamabad.
- Moqbel, A., & Wang, Y. (2011). Carbonate reservoir characterization with lithofacies clustering and porosity prediction. *Journal of Geophysics and Engineering*, *8*, 592–598.
- Parsopoulos, K. E., & Vrahatis, M. N. (2004). On the computation of all global minimizers through particle swarm optimization. *IEEE Transactions on Evolutionary Computation*, *8*, 211–224.
- Pramanik, A. G., Singh, V., Vig, R., Srivastava, K., & Tiwary, D. N. (2004). Estimation of effective porosity using geostatistics and multi-attribute transforms: A case study. *Geophysics*, *69*, 352–372.
- Quadri, S. V. (1986). Hydrocarbon prospects of southern Indus Basin, Pak. *AAPG Bulletin*, *70*(6), 730–747.
- Rickman, R., Mullen, M. J., Petre, J. E., Grieser, W. V., & Kundert, D. (2008). A practical use of shale petrophysics for stimulation design optimization: All shale plays are not clones of the Barnett Shale. In *SPE annual technical conference and exhibition*.
- Russell, B. H. (1988). *Introduction to seismic inversion methods* (p. 86). Tulsa, OK: Society of Exploration Geophysicists.
- Russell, B. H. (2004). *The application of multivariate statistics and neural networks to the prediction of reservoir parameters using seismic attributes*. Ph.D. Dissertation. University of Calgary, Alberta.
- Sancevero, S. S., Remacre, A. Z., Portugal, R. S., & Mundim, E. C. (2005). Comparing deterministic and stochastic seismic inversion for thin-bed reservoir characterization in a turbidite synthetic reference model of Campos Basin, Brazil. *Leading Edge*, *24*(11), 1094–1179.
- Sheikh, N., & Giao, P. (2017). Evaluation of shale gas potential in the lower cretaceous sembar formation, the southern Indus Basin Pakistan. *Journal of Natural Gas Science and Engineering*, *44*, 162–176.
- Singh, A., & Biswas, A. (2016). Application of global particle swarm optimization for inversion of residual gravity anomalies over geological bodies with idealized geometries. *Natural Resources Research*, *25*, 297. <https://doi.org/10.1007/s11053-015-9285-9>.
- Singha, D. K., & Chatterjee, R. (2014). Detection of overpressure zones and a statistical model for pore pressure estimation from well logs in the Krishna-Godavari Basin, India. *Geochemistry, Geophysics, Geosystems*, *15*, 1009–1020.
- Soubotcheva, N. (2006). *Reservoir property prediction from well-logs, VSP and multicomponent seismic data: Pikes Peak heavy oilfield, Saskatchewan*. M.Sc. Thesis, Department of Geology and Geophysics, University of Calgary, Alberta.
- Walls, J. D., Taner, M. T., Taylor, G., Smith, M., Carr, M., Derzhi, N., et al. (2002). Seismic reservoir characterization of a U.S. midcontinent fluvial system using rock physics, poststack seismic attributes, and neural networks. *The Leading Edge*, *21*, 428–436.
- Yasin, Q., Du, Q., & Ismail, A. (2019). A new integrated workflow for improving permeability estimation in a highly heterogeneous reservoir of Sawan Gas Field from well logs data. *Geomechanics and Geophysics for Geo-Energy and Geo-Resources*, *5*, 121–142.
- Yasin, Q., Du, Q., Sohail, G. M., & Ismail, A. (2017). Impact of organic contents and brittleness indices to differentiate the brittle-ductile transitional zone in shale gas reservoir. *Geosciences Journal*, *21*, 779–789.
- Yasin, Q., Du, Q., Sohail, G. M., & Ismail, A. (2018). Fracturing index-based brittleness prediction from geophysical logging data: Application to Longmaxi shale. *Geomechanics and Geophysics for Geo-Energy and Geo-Resources*, *4*(4), 301–325.